5. BURNING-PLASMA SIMULATIONS

Farrokh Najmabadi
William P. Kelleher

Charles G. Bathke
Ronald L. Miller
Ken A. Werley

Patrick I. H. Cooke
Erik L. Vold

Contents

5. BURNING-PLASMA SIMULATIONS

5.1. INTRODUCTION

Extensive studies of the TITAN burning plasma have been performed in order to analyze the plasma behavior and performance (*e.g.*, equilibrium, stability, and transport), and to study key plasma-support systems (*e.g.*, current drive, fueling, impurity control, and particle exhaust). As a whole, these analyses provided detailed descriptions of the burning plasma for all engineering activities and design efforts. The results also provided information to the system analysis activity for improving parametric systems models that were then used to generate new cost-optimized design points for further conceptual design and analysis.

The TITAN burning-plasma simulations incorporate the latest understanding and models developed for reversed-field pinches (RFPs), as is summarized in Section 2; in several cases, new and improved models had to be developed for the TITAN study. Because of the relative lack of theoretical and experimental data bases for RFPs, the sensitivity of the design point to various physics assumptions has also been investigated (Section 3.4.2). A detailed description of the necessary R&D areas for compact RFP reactors has also been produced and is reported in Section 8.

The TITAN burning-plasma simulations include analyses of the equilibrium and stability of the TITAN plasma (Section 5.2). These equilibrium analyses were performed using a large-aspect-ratio approximation. Two-dimensional equilibrium analysis, however, was also performed to substantiate the accuracy of such an approximation for the TITAN effort. The TITAN plasma operates with a highly radiative core plasma, deliberately doped with xenon impurities, to reduce the heat flux on the divertor plates. Therefore, one-dimensional transport simulations of the TITAN core plasma were performed to study the behavior of highly radiative core plasmas and are reported in Section 5.3.

The characteristics of the edge plasma have been of major importance in driving the TITAN design and extensive simulations of the edge plasma have been undertaken during the study. The main objectives of this work are to predict the plasma conditions at the first wall and divertor target, to provide specifications for the engineering design of these components, and to estimate the requirements for particle removal. To obtain a self-consistent view of the behavior of the plasma and neutral particles, this analysis has

been coupled to the modeling of the core plasma (Section 5.3) and the neutral particle transport (Section 5.5). An overview of fueling requirements for the TITAN designs is reported in Section 5.6, and the summary and conclusions of the activities are given in Section 5.7.

Although two separate fusion-power-core designs were studied for the TITAN reactor, lithium cooled for TITAN-I and an aqueous solution of a lithium salt as the coolant and breeder for TITAN-II, both designs had the same plasma parameters. Therefore, most of the burning-plasma simulation effort was not duplicated and, although there are certain references specifically to the TITAN-I design, only minor modifications would be required for TITAN-II.

5.2. EQUILIBRIUM AND STABILITY

The analysis of equilibrium and stability in RFPs usually invokes the large-aspect-ratio (straight cylinder) approximation. Such a model encompasses z-pinches ($q = 0$), θ-pinches ($q \rightarrow \infty$), large-aspect-ratio tokamaks ($q > 1$), and RFPs ($q < 1$). The safety factor, $q(r) \equiv rB_\phi/RB_\theta$, where B_ϕ and B_θ are, respectively, toroidal and poloidal field, and r and R are measured, respectively, in directions of plasma minor (r_p) and major (R_T) radii. The radial pressure balance in these systems is described by:

$$\frac{d}{dr}\left(p + \frac{B_\phi^2 + B_\theta^2}{2\,\mu_0}\right) + \frac{B_\theta^2}{\mu_0\, r} \;=\; 0\,, \tag{5.2-1}$$

where p is the plasma pressure and μ_0 is the permeability of free space. The equilibrium profiles are then subjected to stability analysis via the energy principle [1] or normal-mode technique.

For a toroidal system, equilibrium also requires the compensation of the outward force from the plasma pressure and the plasma current (poloidal-field pressure). Either a perfectly conducting wall, a vertical field produced by the external circuits, or a combination of both, is necessary for equilibrium. The required value of this vertical field is given by Shafranov [2],

$$B_V \;=\; \frac{\mu_0\, I_\phi}{4\pi\, R_T}\left[ln\left(\frac{8R_T}{r_p}\right) + \beta_\theta + \frac{l_i}{2} - 1.5\right]\,, \tag{5.2-2}$$

where l_i is the plasma internal inductance per unit length.

In principle, some information on the current and pressure profiles is required to find the equilibrium magnetic-field profiles. Because of the strong tendency for RFPs to relax,

the field distributions obtained in modern experiments are near-minimum-energy states. The theory of relaxed states predicts the condition,

$$\nabla \times \mathbf{B} = \mu \mathbf{B}\,, \tag{5.2-3}$$

with $\mu = \mu_0 J_{||}/B$ spatially uniform across the plasma, leading to Bessel-function model (BFM) field profiles. However, a constant μ (or constant $J_{||}/B$) implies large parallel current density near the wall in a region of cold, resistive plasma. A μ profile that is nearly constant over the bulk of the plasma and decreases in the outer region to match the practical $\mu(r_p) = 0$ condition eliminates the unphysical features of the BFM. Such μ profiles are observed in RFP experiments.

Combining Equations 5.2-1 and 5.2-2 results in

$$-\frac{dB_\phi}{dr} = \mu(r)\,B_\theta(r) + \mu_0 \frac{dp}{dr}\frac{B_\phi}{B^2} = \mu_0\,J_\theta(r)\,, \tag{5.2-4}$$

$$-\frac{1}{r}\frac{d}{dr}(r\,B_\theta) = \mu(r)\,B_\phi(r) - \mu_0 \frac{dp}{dr}\frac{B_\theta}{B^2} = \mu_0\,J_\phi(r)\,. \tag{5.2-5}$$

These equations are solved to obtain profiles of magnetic field and current density in the plasma. Values of plasma internal inductances, required vertical field, and ohmic losses in the plasma can then be computed. This information is used for analyses of steady-state burn point, magnetics, and the transient operation (Section 6).

We denote normalized profiles by "hats," *i.e.*, $\mu(r) \equiv \mu(0)\,\hat{\mu}(r)$, $p(r) \equiv p(0)\,\hat{p}(r)$, *etc.*, with $\hat{\mu}(0) = \hat{p}(0) = \ldots = 1$. Then, defining $x \equiv r/r_p$, Equations 5.2-4 and 5.2-5 can be written as

$$-\frac{dB_\phi}{dx} = r_p\,\mu(0)\,\hat{\mu}(x)\,B_\theta(x) + \mu_0\,p(0)\,\frac{d\hat{p}}{dx}\frac{B_\phi}{B^2}\,, \tag{5.2-6}$$

$$\frac{dB_\theta}{dx} + \frac{B_\theta}{x} = r_p\,\mu(0)\,\hat{\mu}(x)\,B_\phi(x) - \mu_0\,p(0)\,\frac{d\hat{p}}{dx}\frac{B_\theta}{B^2}\,, \tag{5.2-7}$$

with the following boundary conditions

$$B_\theta(x=0) = 0\,, \tag{5.2-8}$$

$$B_\theta(x=1) = \frac{\mu_0\,I_\phi}{2\,r_p}\,, \tag{5.2-9}$$

$$\lim_{x\to 0}\frac{dB_\theta}{dx} = \lim_{x\to 0}\frac{B_\theta}{x} = \frac{1}{2}\,r_p\,\mu(0)\,B_\phi(0)\,, \tag{5.2-10}$$

$$\lim_{x\to 0}\frac{dB_\phi}{dx} = 0\,. \tag{5.2-11}$$

The above equations are solved for given μ and p normalized profiles, poloidal beta $\beta_\theta \equiv 2\mu(0)\langle p\rangle / B_\theta^2(r_p)$ [or $p(0)$], and either the reversal parameter, F, or the pinch parameter, Θ:

$$F \equiv \frac{B_\phi(r_p)}{\langle B_\phi\rangle}, \tag{5.2-12}$$

$$\Theta \equiv \frac{B_\theta(r_p)}{\langle B_\phi\rangle}, \tag{5.2-13}$$

where the average toroidal field within the conducting shell, $\langle B_\phi\rangle$, is defined as

$$\langle B_\phi\rangle = \frac{2}{r_p^2}\int_0^{r_p} B_\phi(r)\, r\, dr\,. \tag{5.2-14}$$

Because of the mixed nature of the boundary conditions (Equations 5.2-8 through 5.2-11), the equilibrium equations are solved by iterating over parameters $B_\phi(0)$ and $\mu(0)$ until values of $B_\theta(r_p)$ and F or Θ match the desired values. Previously, the equilibrium equations were solved for magnetic field values normalized to $B_\phi(0)$ [$\bar{B}_\phi \equiv B_\phi/B_\phi(0)$ and $\bar{B}_\theta \equiv B_\theta/B_\phi(0)$]:

$$\frac{d\bar{B}_\phi}{dx} = -2\Theta_0\,\hat{\mu}(x)\bar{B}_\theta(x) - \frac{\beta_{\phi 0}}{2}\frac{d\hat{p}}{dx}\frac{\bar{B}_\phi}{\bar{B}^2}, \tag{5.2-15}$$

$$\frac{d\bar{B}_\theta}{dx} + \frac{\bar{B}_\theta}{x} = +2\Theta_0\,\hat{\mu}(x)\bar{B}_\phi(x) - \frac{\beta_{\phi 0}}{2}\frac{d\hat{p}}{dx}\frac{\bar{B}_\theta}{\bar{B}^2}, \tag{5.2-16}$$

with boundary conditions, $\bar{B}_\theta(0) = 0$, $d\bar{B}_\theta/dx\ (0) = \Theta_0$, $\bar{B}_\phi(0) = 1$, and $d\bar{B}_\phi/dx\ (0) = 0$. Parameters Θ_0 and $\beta_{\phi 0}$ are defined as

$$\Theta_0 = \frac{1}{2}\mu(0)\, r_p\,, \tag{5.2-17}$$

$$\beta_{\phi 0} = \frac{2\mu_0\, p(0)}{B_\phi^2(0)}\,. \tag{5.2-18}$$

Again, the equilibrium equations are solved by iterating over parameters Θ_0 and $\beta_{\phi 0}$ until values of $B_\theta(r_p)$ and F or Θ match the desired values. Good starting estimates for the iteration process are $\beta_{\phi 0} = 0.5\beta_\theta$ and $\Theta_0 = \Theta$ or $\Theta_0 = 1.5 - F$ (depending on whether Θ of F value is specified).

An alternative has been developed for the TITAN study that is more robust numerically. Normalizing the magnetic field to the value of poloidal field at the plasma edge,

$\tilde{B}_\phi \equiv B_\phi/B_\theta(r_p)$ and $\tilde{B}_\theta \equiv B_\theta/B_\theta(r_p)$, the equilibrium equations can be written as

$$\frac{d\tilde{B}_\phi}{dx} = -2\Theta_0\,\hat{\mu}(x)\tilde{B}_\theta(x) - \frac{\beta_\theta}{2g_p}\frac{d\hat{p}}{dx}\frac{\tilde{B}_\phi}{\tilde{B}^2}\,, \tag{5.2-19}$$

$$\frac{d\tilde{B}_\theta}{dx} + \frac{\tilde{B}_\theta}{x} = +2\Theta_0\,\hat{\mu}(x)\tilde{B}_\phi(x) - \frac{\beta_\theta}{2g_p}\frac{d\hat{p}}{dx}\frac{\tilde{B}_\theta}{\tilde{B}^2}\,, \tag{5.2-20}$$

with the boundary conditions, $\tilde{B}_\theta(0) = 0$, $d\tilde{B}_\theta/dx\ (0) = \Theta_0\,\tilde{B}_\phi(0)$, and $d\tilde{B}_\phi/dx\ (0) = 0$. Parameters Θ_0 and $\beta_{\phi 0}$ are defined as before (Equations 5.2-17 and 5.2-18) and g_p is the pressure profile factor,

$$g_p \equiv \frac{\langle p\rangle}{p(0)}\,. \tag{5.2-21}$$

As before, these equilibrium equations are solved by iterating over parameters Θ_0 and $\tilde{B}_\phi(0)$ until values of $\tilde{B}_\theta(r_p) = 1$ and F or Θ match the desired values. Good starting estimates for the iteration process are $\tilde{B}_\phi(0) = \sqrt{2/g_p}$ (corresponding to $\beta_{\phi 0} = 0.5\beta_\theta$) and $\Theta_0 = \Theta$ or $\Theta_0 = 1.5 - F$ (depending on whether Θ of F value is specified). The above equations are solved by standard predictor/corrector method over a uniform mesh for x since magnetic field profiles are then integrated to find the plasma internal inductance as is described below. The iteration on Θ_0 and $\tilde{B}_\phi(0)$ are performed using Newton-Raphson method. It is found that using an 80-point mesh will yield accuracies of $< 10^{-6}$ in computed values of plasma inductances and ohmic dissipation in the plasma (error in the field and current density profiles are considerably smaller). The Newton-Raphson iteration procedure is also found to converge after 3 to 5 iterations.

It is important to note that Equations 5.2-19 and 5.2-20 show that the profiles of magnetic field and current density only depend on the profiles of μ and pressure, the poloidal beta, and F or Θ values. These profiles are independent of the plasma current and/or plasma minor radius. This observation is also true for plasma internal inductances and plasma-resistance composite-profile factor, g_{OHM}. The plasma internal inductance per unit length, $l_{i,P} \equiv L_{i,p}/(2\pi R_T)$, can be written as

$$l_{i,P} = l_{i,p} + l_{i,t} = \frac{2}{I_\phi^2}W_p + \frac{2}{I_\phi^2}\left(W_t - \frac{\Phi^2}{4\pi\,R_T\,L_0}\right)\,, \tag{5.2-22}$$

where $l_{i,p}$ and $l_{i,t}$ are, respectively, poloidal and toroidal plasma internal inductances, and

$$W_i = \frac{\pi}{\mu_0}\int_0^{r_p} B_i^2\,r\,dr\,, \qquad (i = p \text{ or } t)\,, \tag{5.2-23}$$

$$\Phi = 2\pi \int_o^{r_p} B_\phi \, r \, dr \,, \tag{5.2-24}$$

$$L_0 = \frac{\mu_0 \, r_p^2}{2R_T} \,. \tag{5.2-25}$$

Using the normalized field profiles, $\tilde{B}_\phi$ and $\tilde{B}_\theta$, the internal inductances per unit length can be written as

$$l_{i,p} = \frac{\mu_0}{2\pi} \int_0^1 \tilde{B}_\theta^2(x) \, x \, dx \,, \tag{5.2-26}$$

$$l_{i,t} = \frac{\mu_0}{2\pi} \left[\int_0^1 \tilde{B}_\phi^2(x) \, x \, dx - 2 \left(\int_0^1 \tilde{B}_\phi(x) \, x \, dx \right)^2 \right] . \tag{5.2-27}$$

The equilibrium profiles are also used to compute the plasma-resistance composite-profile factor, g_{OHM}, which is defined through

$$P_{OHM} = g_{OHM} \, \langle \eta_\parallel \rangle \, \langle J_\parallel \rangle^2 \,, \tag{5.2-28}$$

where P_{OHM} is the ohmic heating in the plasma and $\langle \eta_\parallel \rangle$ is classical resistivity of the plasma which is computed based on the average electron temperature, T_e,

$$\langle \eta_\parallel \rangle = 0.51 \, \frac{4\sqrt{2\pi}}{3} \, \frac{m_e^{1/2}}{k^{3/2}} \left(\frac{e}{4\pi \, \epsilon_0} \right)^2 \frac{Z_{eff}}{N(Z_{eff})} \, \lambda_e i \, T_e^{-3/2} \,, \tag{5.2-29}$$

$$N(Z_{eff}) \simeq 1 + 0.718 \left(\frac{Z_{eff} - 1}{Z_{eff}} \right)^2 \,, \tag{5.2-30}$$

where m_e is the electron mass, k is the Boltzmann constant, ϵ_0 is the vacuum permittivity, Z_{eff} is the effective plasma charge, and λ_{ei} is the Coulomb logarithm. Substituting in Equation 5.2-28 for P_{OHM} from

$$P_{OHM} = \frac{2}{r_p^2} \int_0^{r_p} \eta_\parallel(r) J_\parallel^2(r) \, r \, dr \,, \tag{5.2-31}$$

and noting $J_\parallel = \mu(r) B(r) / \mu_0$, the plasma-resistance composite-profile factor, which includes the effect of the temperature profile as well as the field-line screw-up factor, is

$$g_{OHM} = 2 \, \Theta_0^2 \, g_T^{3/2} \int_0^1 \frac{\hat{\mu}^2(x)}{\hat{T}^{3/2}(x)} \, \tilde{B}^2(x) \, x \, dx \,. \tag{5.2-32}$$

Note that values of $l_{i,p}$, $l_{i,t}$, and g_{OHM} are all independent of plasma current and size and only depend on μ and p profiles, β_θ, and F or Θ values.

For the analysis of the TITAN plasma, two distinct sets of μ and p profiles have been used. For start-up and transient calculation, a standard set of profiles,

$$\mu(r) = \mu(0)\left[1 - (r/r_p)^8\right], \tag{5.2-33}$$

$$n(r) = n(0)\left[1 - (r/r_p)^{2.5}\right], \tag{5.2-34}$$

$$T(r) = T(0)\left[1 - (r/r_p)^4\right], \tag{5.2-35}$$

are used. At steady-state full-power operation, the TITAN plasma is deliberately doped with a trace amount of Xe impurity to enhance core-plasma radiation and to reduce the heat load on the divertor target plates. One-dimensional transport analysis (Section 5.3) has been performed and the following plasma profiles were obtained:

$$\mu(r) = 2.843\left[1 - 0.44(r/r_p)^6 - 0.56(r/r_p)^8\right], \tag{5.2-36}$$

$$T_e(r) = \begin{cases} 14.40 - 46.94(r/r_p)^{2.8504} & (0. < r/r_p < 0.25) \\ 16.07 - 10.29(r/r_p) & (0.25 < r/r_p < 0.833) \\ 8.111 - 7.886(r/r_p)^{14.025} & (0.833 < r/r_p < 1) \end{cases}, \tag{5.2-37}$$

$$n(r) = 1.23 \times 10^{21}\left[1 - 0.8577(r/r_p)^{3.44}\right]. \tag{5.2-38}$$

These profiles have been used in the burning-plasma simulations.

Figures 5.2-1 through 5.2-4 show, respectively, the normalized profiles of plasma parameters (n, T, P, and μ), magnetic field, current density, and safety factor, q, for both sets of profiles. Table 5.2-I compares the values of plasma profile factors and plasma internal inductances for both profiles. These equilibrium profiles and parameters are computed for $\beta_\theta = 0.2$ and $F = -0.1$. Values of magnetic-field strength and current density are also given for $r_p = 0.6\,\mathrm{m}$ and $I_\phi = 17.8\,\mathrm{MA}$.

The above cylindrical equilibrium calculations have been used extensively for simulation of the TITAN plasma. The accuracy of this model has been checked against equilibrium calculations performed by the computer code NEQ [3]. Figure 5.2-5 illustrates the flux surfaces of the TITAN reactors. The equilibrium parameters computed by NEQ are in good agreement with those reported in Table 5.2-I.

The equilibrium pressure profile described by Equation 5.2-1 must be subjected to stability analysis using the energy principle [1] or normal-mode analysis. Necessary conditions for stability against ideal-MHD current-driven modes have been derived by Robinson [4] on the basis of the energy principle [1]. The necessary condition can be expressed

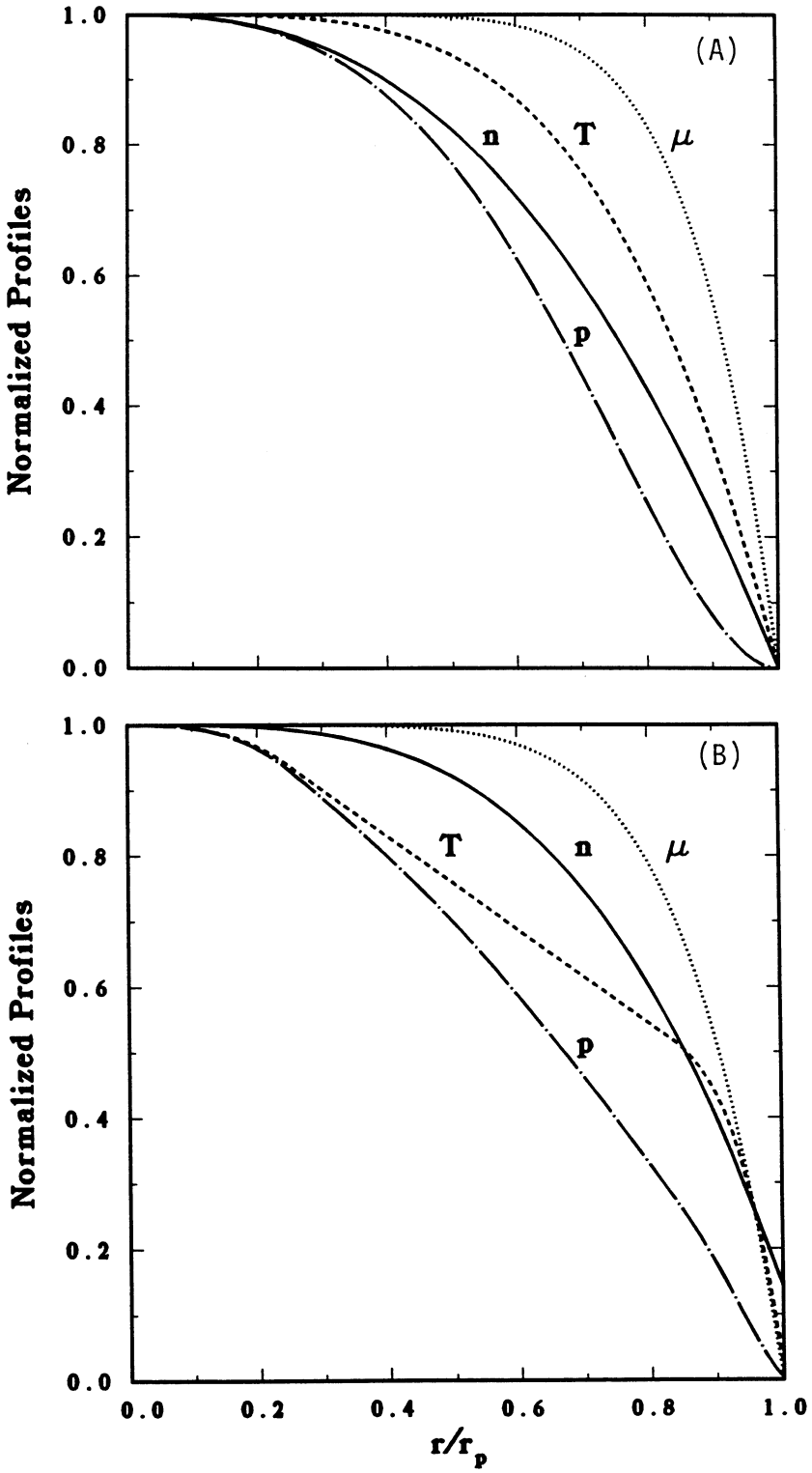

Figure 5.2-1. Plasma density (n), temperature (T), pressure (p), and μ profiles for power (A) and radiative profiles (B).

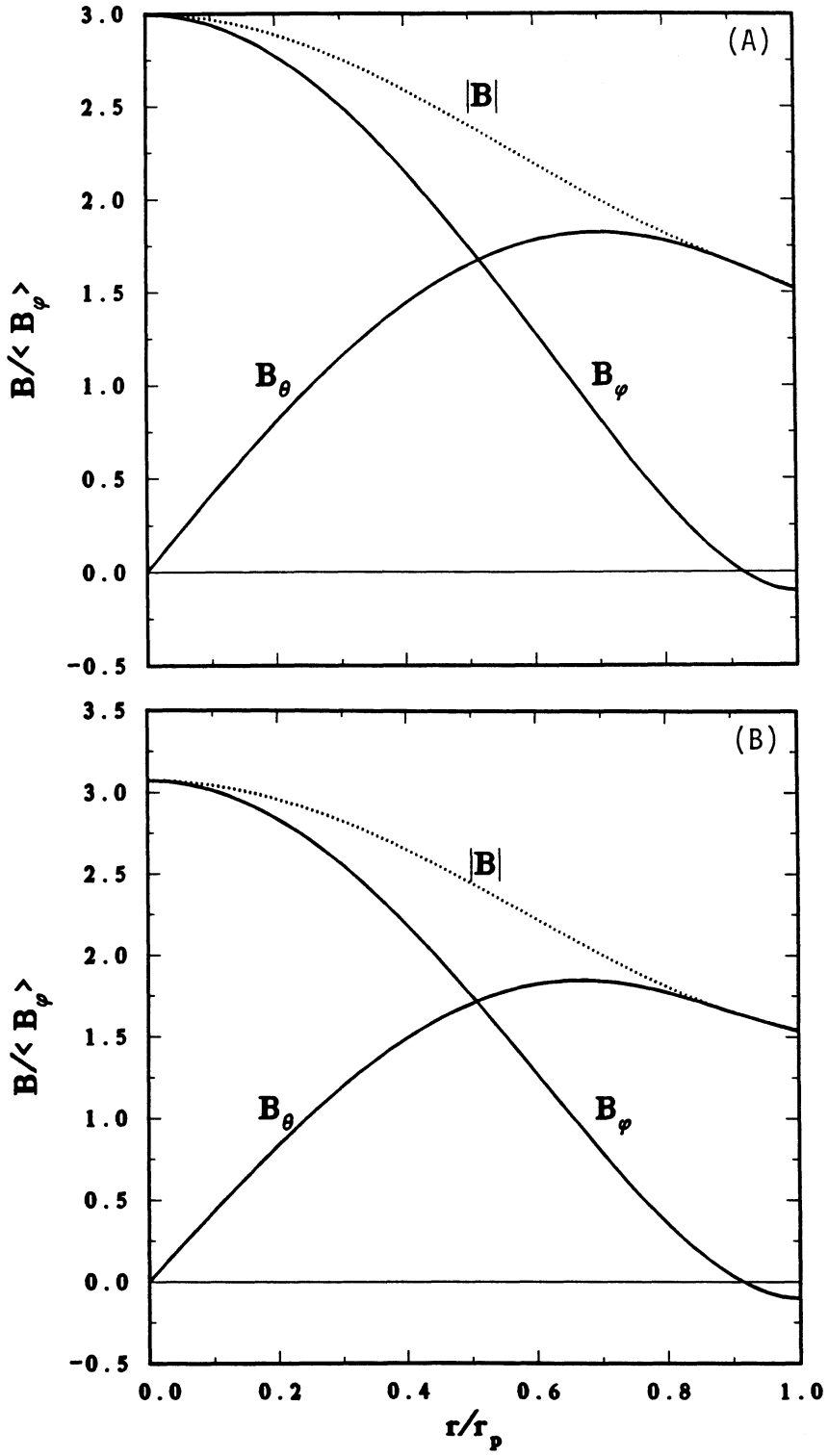

Figure 5.2-2. Equilibrium profiles of magnetic field for power (A) and radiative profiles (B).

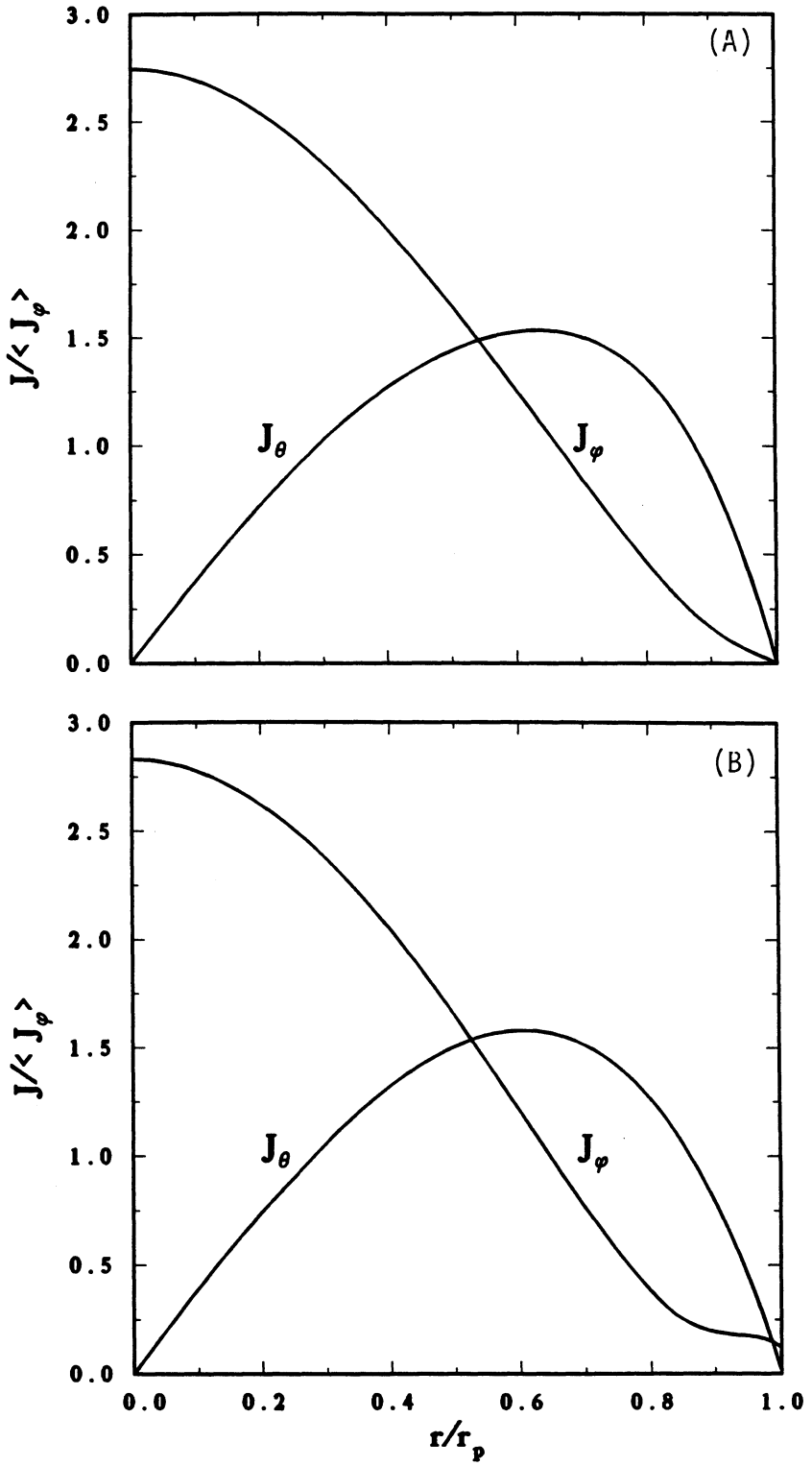

Figure 5.2-3. Equilibrium profiles of plasma current density for power (A) and radiative profiles (B).

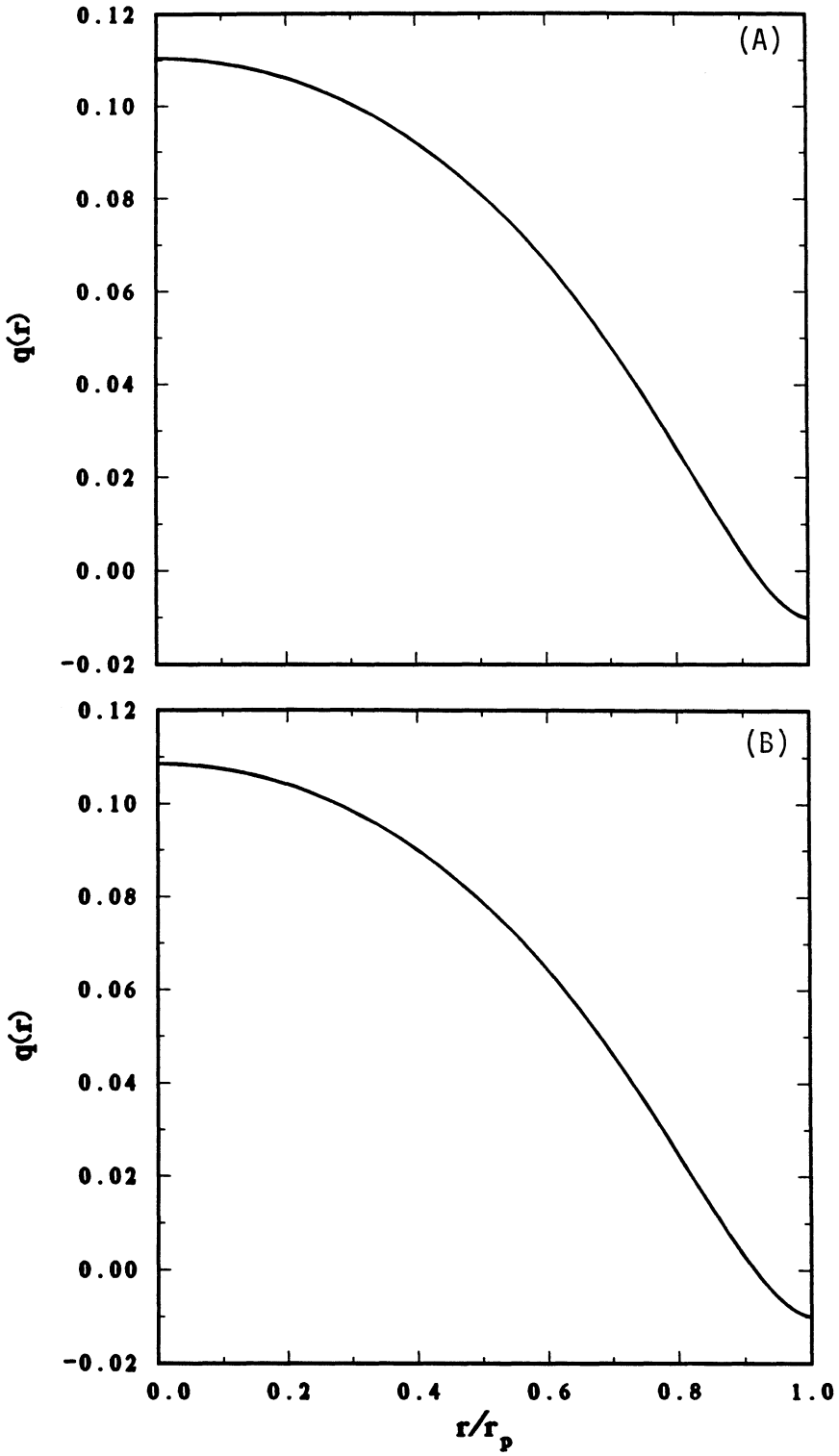

Figure 5.2-4. Equilibrium profiles of the safety factor for power (A) and radiative profiles (B).

Table 5.2-I.

EQUILIBRIUM PARAMETERS OF TITAN PLASMA

Parameter	Power Profiles[a]	Radiative Profiles [b]
Poloidal beta, β_θ	0.2	0.2
Reversal parameter, F	−0.1	−0.1
Pinch parameter, Θ	1.522	1.538
Safety factor, q		
On axis	0.110	0.109
At plasma edge	−0.011	−0.010
Field-line pitch, P		
On axis	0.430	0.423
At plasma edge	−0.039	−0.039
Plasma internal inductance per unit length (H/m)		
Poloidal, $l_{i,p}$	1.136×10^{-7}	1.140×10^{-7}
Toroidal, $l_{i,t}$	3.724×10^{-8}	3.824×10^{-8}
Total, $l_{i,P}$	1.508×10^{-7}	1.522×10^{-7}
Plasma-resistance profile factor, g_{OHM}	3.419	2.918
Poloidal field at plasma edge, $B_\theta(r_p)$ (T)[c]	5.93	5.93
Toroidal field[c]		
On axis, $B_\phi(0)$ (T)	11.69	11.85
At plasma edge, $B_\phi(r_p)$ (T)	−0.390	−0.386
Average, $\langle B_\phi \rangle$ (T)	3.90	3.86
Toroidal current density[c]		
On axis, $J_\phi(0)$ (MA/m^2)	43.2	44.6
At plasma edge, $J_\phi(r_p)$ (MA/m^2)	0.	1.90
Average, $\langle J_\phi \rangle$ (MA/m^2)	15.7	15.7

(*a*) Profiles of plasma n, T, and μ are given in Equations 5.2-33 through 5.2-35.

(*b*) Profiles of plasma n, T, and μ are given in Equations 5.2-36 through 5.2-38.

(*c*) Values for $r_p = 0.6\,\text{m}$ and $I_\phi = 17.8\,\text{MA}$.

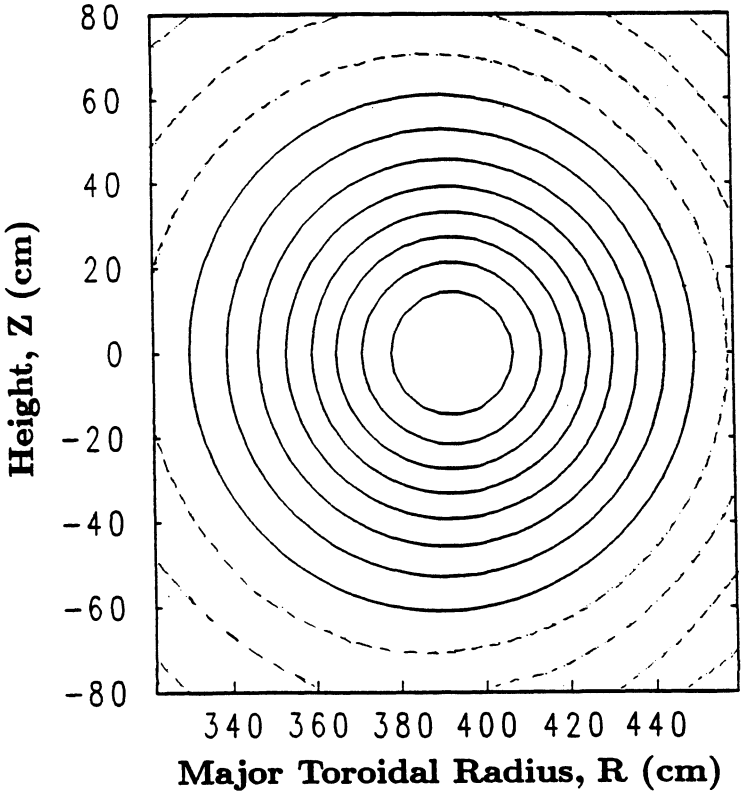

Figure 5.2-5. Equilibrium flux surface for the TITAN plasma computed by NEQ [3].

as $| P(r_w) | < 3P(0)$, where $P \equiv qR$ is the field-line pitch and r_w is the location of the conducting wall. This condition can be approximately expressed as follows:

$$\left(\frac{r_w}{r_p}\right)^2 < 3\left|\frac{B_\phi(0)}{B_\phi(r_w)}\right|, \tag{5.2-39}$$

$$\Phi > 0, \tag{5.2-40}$$

where Φ is the total toroidal flux inside the conducting wall. These conditions do not include a vacuum boundary and require that both the amplitude and the region of the field reversal not be large.

In summary, the conducting wall should be close to the plasma to stabilize current-driven modes. Furthermore, stability against current-driven modes also excludes a pitch minimum in the plasma. These conditions are usually well satisfied for experimental profiles and are also monitored and satisfied for the profiles calculated for the TITAN designs. The necessary conditions given by Equations 5.2-39 and 5.2-40 are in practice close to being sufficient. Based on ideal-MHD theory, RFP profiles are possible with plasma beta values as high as 0.3.

The ideal-MHD theory assumes a zero plasma resistivity. This assumption constrains magnetic field lines to be "frozen" in the plasma, thereby limiting the class of potentially unstable modes. Resistive-MHD stability analysis has to be performed to provide a more realistic picture of the plasma behavior [4]. In general, the criteria for resistive stability are more stringent, and a closer fitting conducting wall and a lower value of β generally result. A detailed analysis of current-driven resistive tearing modes has been made [5] and stable RFP configurations have been found with $\beta \simeq 0.2$. These configurations, however, have been found to be unstable to the so-called resistive g-modes (the "g" is used to emphasize the "gravity" analogy). Moreover, analyses show that resistive g-modes can become unstable for pressure gradients substantially smaller than those needed to drive ideal-MHD instabilities. These resistive g-modes are localized and may ultimately affect the confinement time. In fact, certain theoretical estimates of the confinement time have been proposed that are based on transport along stochastic field lines created by resistive g-mode turbulence [6] and are discussed in Section 2.

The current-driven MHD instabilities have more recently been analyzed for an RFP in contact with a perfectly conducting wall [7], and even more recently for conditions where a vacuum annulus exists between the RFP and the conducting wall [8]. Figure 5.2-6 gives an example of a stability diagram for the fastest growing $m = 1$ mode as a function of the μ-profile shape factors, $\mu(0)$ and α, as given in Equation 5.2-4. These analytic results show that a completely stable region exists for ideal and resistive current-driven modes in an RFP over a range of $\Theta \simeq \Theta_o$ and degrees of current-density peaking, and for a range of free-boundary conditions, $\delta_v \simeq (r_w - r_p)/r_p$. Generally, the external $m = 1$ modes do not appear to be significant. These external modes occur for deep-reversal conditions that rarely arise for most experiments and are not of interest for reactors because of cost and technology demands (Section 8). A lower limit on $q(0)\,A = \Theta_o \geq 2/3$ is identified which weakly depends on the profile exponent α. This lower limit is associated with the internal $m = 1$ resistive mode, and imposes an upper limit on the on-axis current density [7,8] of $J_\phi(0) \leq 3B_\phi(0)/(\mu_o\, r_p)$. As noted in Reference [7], resistive diffusion tends to peak the on-axis current, lowering $q(0)$ to below this critical limit and exciting internal current-driven instabilities, redistributing (*i.e.,* flattening) the current-density profile, and recovering the initial configuration that is stable to tearing modes. Hence, the field profiles in RFPs are a result of periodic relaxations that oppose processes related to resistive diffusion; such oscillations around near fields have been observed in a number of large-Θ RFP discharges [9,10].

Given the above considerations, detailed stability analyses of TITAN profiles were not performed. Rather, a poloidal beta of $\beta_\theta = 0.23$ (corresponding to fuel ion beta of

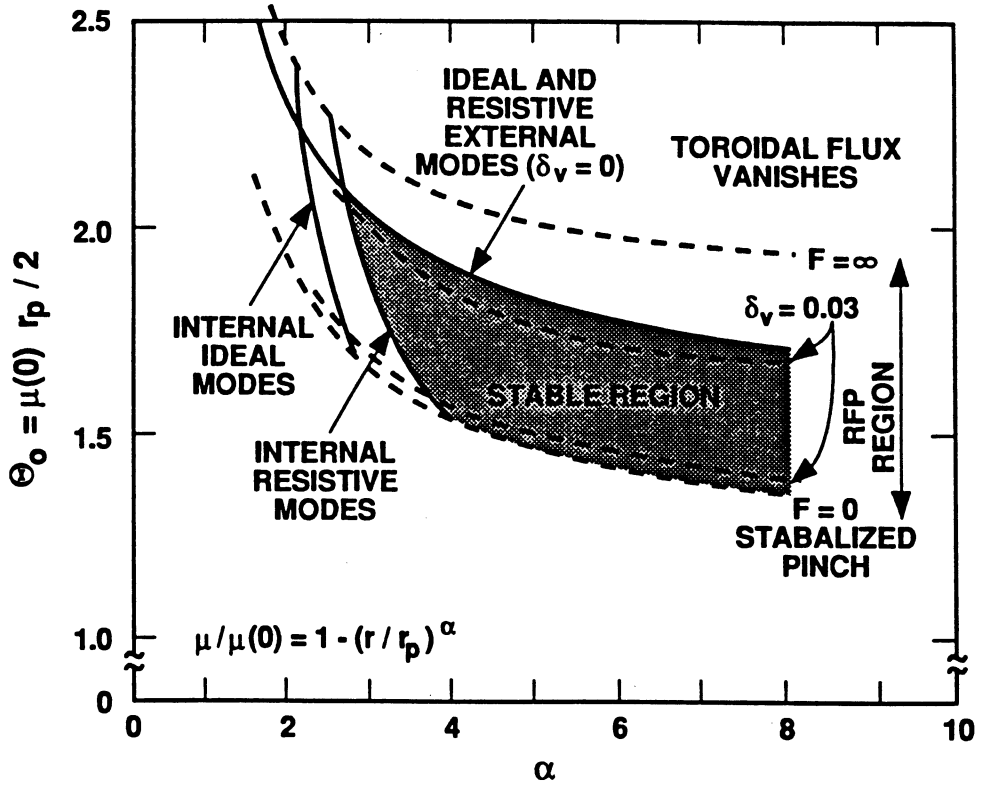

Figure 5.2-6. Stability diagram for $m = 1$ internal (inside reversal layer) and external resistive current-driven modes for an RFP with a vacuum annulus equal to $\delta_v = 0.0$ and 0.3 of the plasma radius [7,8].

0.2) was assumed. The sensitivity of the reference design to achievable stable value of poloidal beta was also studied and reported in Section 3.4.2.

Finally, the existence and role of a close-fitting conducting shell that surrounds the RFP strongly impacts all physics and engineering aspects of the design. The data base for RFP operation with resistive shells is summarized in Section 2.3.9. However, the need for and characteristics of a conducting shell with electrical breaks and its impact on RFP formation and start-up, confinement, current drive, and impurity control represent an important but inadequately mapped issue for the RFP. Because of the lack of data base, the TITAN study has circumnavigated this issue numerous times by assuming that the first wall and blanket would act as the conducting shell.

5.3. CORE-PLASMA SIMULATIONS

A 1-D RFP plasma burn code, RFPBURN [11,12], has been used to study transport and other 1-D effects in the bulk plasma of the TITAN reactors. While a 0-D plasma and circuits code has been used as the main tool to examine TITAN reactor transients (Section 6), RFPBURN supplements the 0-D model by examining 1-D aspects of local transport assumptions, impurity radiation with beta limits, pellet refueling, dynamo, and current drive. A brief summary of RFPBURN models is given in Section 5.3.1.

Experimental observation of the scaling of RFP plasma pressure with the toroidal current, $nT_e(0) \propto I_\phi^2$, is suggestive of operation near a beta limit. Under this condition, the intrinsic transport would adjust by MHD activity, radiation, or other mechanism to lose energy at a rate sufficient to maintain β_θ constant. To test this hypothesis, experiments were performed on ZT-40M by adding trace quantities of krypton impurity [13] to enhance the radiative losses. Krypton was chosen to maximize the ratio of radiated power to the ohmic heating power. It was found that as the impurity was injected, the rate of radiation loss, P_{RAD}, was increased but, simultaneously, the ohmic power, P_{OHM}, only slightly increased. Most importantly, β_θ remained constant. This observation suggests that as radiation losses are increased, the non-radiative or "intrinsic" transport losses, P_{NR}, decrease to maintain the beta constant.

A simplified zero-dimensional power-balance model for a steady-state plasma gives $P_{OHM} = P_{RAD} + P_{NR}$. Using the definitions of the global energy-confinement time, τ_E, and a non-radiative (intrinsic) energy-confinement time, τ_E^{NR}, the following expression results:

$$\tau_E^{NR} = \tau_E \left(1 - \frac{P_{RAD}}{P_{RAD} + P_{NR}}\right)^{-1} . \qquad (5.3\text{-}1)$$

For the assumed constant-beta scaling and self-similar profiles of density and electron temperature before and after krypton injection, the values of the total energy loss ($P_{RAD} + P_{NR}$) and τ_E remain unchanged. Equation 5.3-1 indicates that as the radiative losses increase, the non-radiative losses decrease (or τ_E^{NR} increases) to maintain the energy content of the plasma and hold β_θ constant. The data from the krypton impurity experiments are plotted in Figure 5.3-1, and close agreement with predictions of Equation 5.3-1 is indicated.

This characteristic of the RFP is in marked contrast with other confinement schemes such as the tokamak, where increasing the impurity content would increase the total

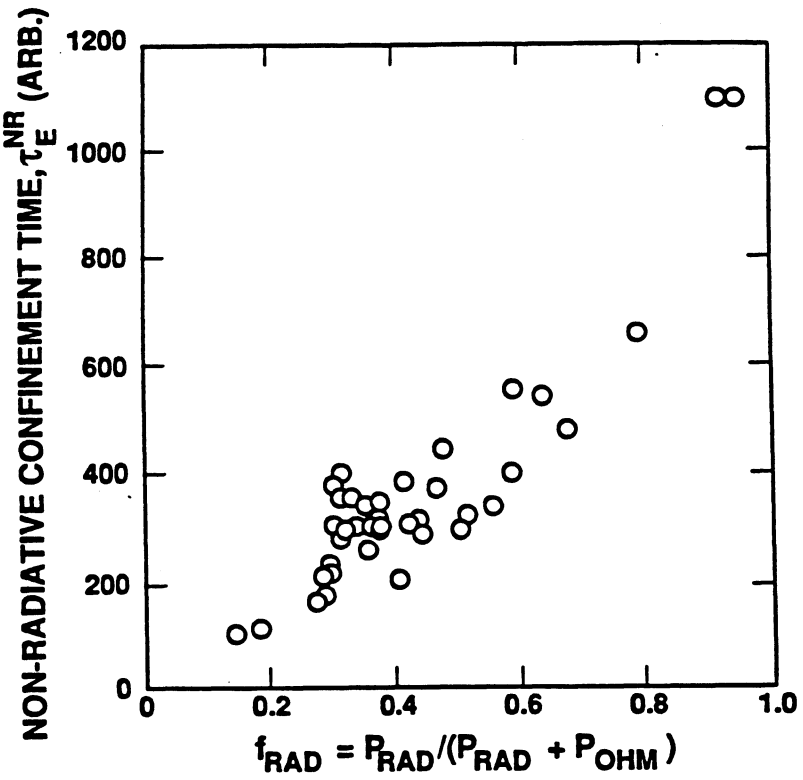

Figure 5.3-1. Scaling of the non-radiative energy-confinement time with the fractional radiative-power loss in the ZT-40M experiments [13].

energy-loss rate and degrade the plasma pressure. Enhanced radiation from a (high) beta-limited plasma is important because it permits first wall designs to receive a higher average (but more uniform) heat flux and to minimize the divertor (or limiter) power loads, thereby optimizing the overall design for the maximum power density while maintaining realistic engineering constraints on all systems.

The RFPBURN code has been used to examine the possibility of seeding the TITAN plasma with impurities in order to enhance the ratio of radiative-to-transport losses and to reduce peak heat loads on the divertor target plates. This analysis has led to the TITAN reference design which is seeded with Xe impurities (Section 5.3.2). The plasma profiles obtained from this 1-D analysis are then used in the 0-D analysis. Additionally, RFPBURN results are coupled to the edge-plasma models to provide self-consistent core/edge-plasma boundary conditions (Section 5.4).

5.3.1. Model

Table 5.3-I summarizes the key features of the RFPBURN code. The 1-D RFPBURN model includes a dynamo electromotive-force term which permits a steady-state normalized profile where $\mu \equiv \mu_o \mathbf{j} \cdot \mathbf{B}/B^2$. The shape of the desired μ profile is determined prior to the application of the 1-D transport model by using the equilibrium solver routine from the Hewett-Freiberg linear resistive-stability code [14] to match the F and Θ values of the 0-D design point. The equilibrium inputs are the μ profile and a normalized pressure profile of the following form:

$$\mu(r) = \mu(0)\left[1 + a_2\,(r/r_p)^2 + a_4\,(r/r_p)^4 + a_6\,(r/r_p)^6 + a_8\,(r/r_p)^8\right], \quad (5.3\text{-}2)$$

$$p(r) = \frac{0.05\,B^2(0)}{\mu_0}\left[1 - 0.9973\,(r/r_p)^2\right]. \quad (5.3\text{-}3)$$

The μ profile is constrained to be a positive monotonic function decreasing to zero at the edge. A parabolic normalized pressure profile was assumed with the on axis and edge values obtained from transport calculations that self-consistently coupled the core and edge plasma.

In order to examine some of the properties of a beta-limited and radiation-dominated reactor-grade plasma, a radiation model with coronal equilibrium and a constant impurity density is assumed. In order to incorporate a soft β limit in a 1-D formulation, the transport coefficients were assumed with the following form:

$$K_e = K_{\perp e}^{cl}\, f(\beta_\theta), \quad (5.3\text{-}4)$$

$$K_i = K_{\perp i}^{cl} + K_e/4, \quad (5.3\text{-}5)$$

$$D = D^{cl}\,[1 + 0.1 f(\beta_\theta)], \quad (5.3\text{-}6)$$

where $K_\perp^{cl}$ and D^{cl} are classical values of the cross-field thermal conductivity and particle diffusivity, and the following function, $f(\beta_\theta)$, is used to model the observed soft β limit:

$$f(\beta_\theta) = \begin{cases} 1 & \beta_\theta \le \beta_{\theta c} \\ g(r)\,\exp\left[(\beta_\theta/\beta_{\theta c})^{15} - 1\right] & \beta_\theta > \beta_{\theta c} \end{cases}, \quad (5.3\text{-}7)$$

$$g(r) = \begin{cases} 1 & r > 0.84 r_p \text{ or } \beta(0) \le 0.11 \\ 1 + 10\left[1 - (r/0.84 r_p)^2\right] & \beta(0) > 0.11 \end{cases}. \quad (5.3\text{-}8)$$

Here, the exponential factor represents the poloidal beta limit. The parabolic factor, $g(r)$, represents an enhanced internal transport that excludes highly peaked temperature profiles caused by highly localized radiation losses. This enhanced internal transport is

consistent with the flat density and temperature profiles observed on ZT-40M [15], which could result either from internal large-scale $m = 1$ current-driven modes, or from "local" β-limit effects. The model uses boundary conditions at r_p that include the toroidal magnetic field and the toroidal loop voltage as well as extrapolation endpoint conditions for the density and temperatures.

Table 5.3-I.

KEY FEATURES OF THE 1-D RFP TRANSPORT CODE, RFPBURN

- The code follows the time-dependent, cylindrical plasma evolution of ion and alpha-particle densities, ion and electron temperatures, and poloidal and axial (toroidal) magnetic fields.
- Physics constraints include Ohm's law, radial pressure balance, and local quasi-neutrality.
- Physical terms include conduction, diffusion, convection, resistive dissipation, fusion reactions, Bremsstrahlung radiation, impurity radiations based on a coronal equilibrium model, a volumetric ion source and/or a pellet injection model, and finally, a simple dynamo model that conserves helicity and allows the RFP configuration to be maintained at steady state.
- Boundary conditions consist of six regularity conditions at the origin ($r = 0$) and six wall conditions that include the toroidal magnetic field, the toroidal voltage, and either extrapolation endpoint or pedestal conditions on the densities and temperatures.
- Global plasma particle and energy balance is followed and used to ensure particle and energy conservation.

5.3.2. Impurity Radiation

The interim TITAN design parameters, as described in Table 5.3-II, were used in this analysis. The computational results are summarized in Table 5.3-III. The required impurity fraction and the resultant Z_{eff} as functions of the core radiation fraction are shown in Figure 5.3-2.

A minimum core-plasma radiation fraction, $f^c_{RAD} = 0.12$, is computed for an $\sim 4\%$ alpha-particle ash with no other impurities. While low-Z impurities such as carbon can radiate the necessary power, a high impurity level ($f_j = 0.04$) is required. For a given plasma beta and plasma current, a large impurity level changes the shape of the plasma profiles and thus the fusion (alpha-particle) power, P_α, as shown in Table 5.3-III. Small increases in I_ϕ, however, result in large increases in P_α and, therefore, design powers can be recovered easily with moderate (5%) increases in I_ϕ. The fusion power can also be increased by trading off density with temperature. Such optimizations can best be done at the 0-D level of analysis. The high value of $Z_{eff} = 2$ for the carbon impurity would double the current-drive power requirements.

High-Z impurities, such as xenon, require a much smaller impurity concentration and give lower values of Z_{eff} [*e.g.*, $Z_{eff}(0) = 1.3$ for Xe and the Z_{eff} decreases with radius]. High-Z impurities, therefore, are favored for enhancing the plasma radiation fraction. In addition to determining that high-Z impurities can radiate the same power as low-Z impurities with a lower Z_{eff} (and hence, P_{OHM}), an additional study evaluated the optimal plasma temperature for minimizing the ohmic dissipation, P_{OHM}. Results are presented in Table 5.3-IV for a plasma with a fixed β_θ, I_ϕ, and f^c_{RAD}. Plasmas with large radiation fractions and a significant xenon-impurity density ($10^{17} - 10^{18}\,\mathrm{m}^{-3}$), actually have higher dissipation at higher plasma temperatures because Z_{eff} increases more quickly than $T_e^{-3/2}$ decreases. Minimizing P_{OHM} is crucial for reducing current drive requirements (Section 7). The optimum operating temperature for a highly radiative plasma, therefore, is the minimum required to produce the required fusion power (8 to 10 keV) while minimizing OFCD power requirements and cost.

The profiles of plasma parameters for these 1-D simulations are uncertain since local transport is not known. But the highly localized radiative losses in the outer regions of the plasma are not expected to change the plasma profiles dramatically if a local beta limit or some other source of rapid transport in the plasma core exists. It is noted that if the transport in the plasma core is too low, then high radiation losses at the plasma edge could result in a temperature collapse of the entire plasma column as the cold, radiating edge propagates inward.

Table 5.3-II.

REACTOR CONDITIONS USED
FOR THE IMPURITY SEEDING ANALYSIS

Plasma minor radius, r_p (m)	0.71
Plasma major toroidal radius, R_T (m)	3.93
Toroidal current, I_ϕ (MA)	18.0
Average ion density, n_i (m^{-3})	8.67×10^{20}
Critical poloidal beta, $\beta_{\theta c}$	0.19

Table 5.3-III.

STEADY-STATE RADIATION RESULTS OF THE 1-D MODEL

	None	C	Xe	U
Z_j	–	12.	54.	92.
f_j	0.0	4×10^{-2}	1×10^{-4}	3×10^{-5}
Z_{eff}	1.04	2.0	1.3	1.15
τ_E^{NR} (s)	0.64	7.9	1.2	1.8
τ_E (s)	0.25	0.53	0.35	0.35
P_α (MW)	336.	233.	306.	321.
f_{RAD}^c	0.12	0.76	0.71	0.81

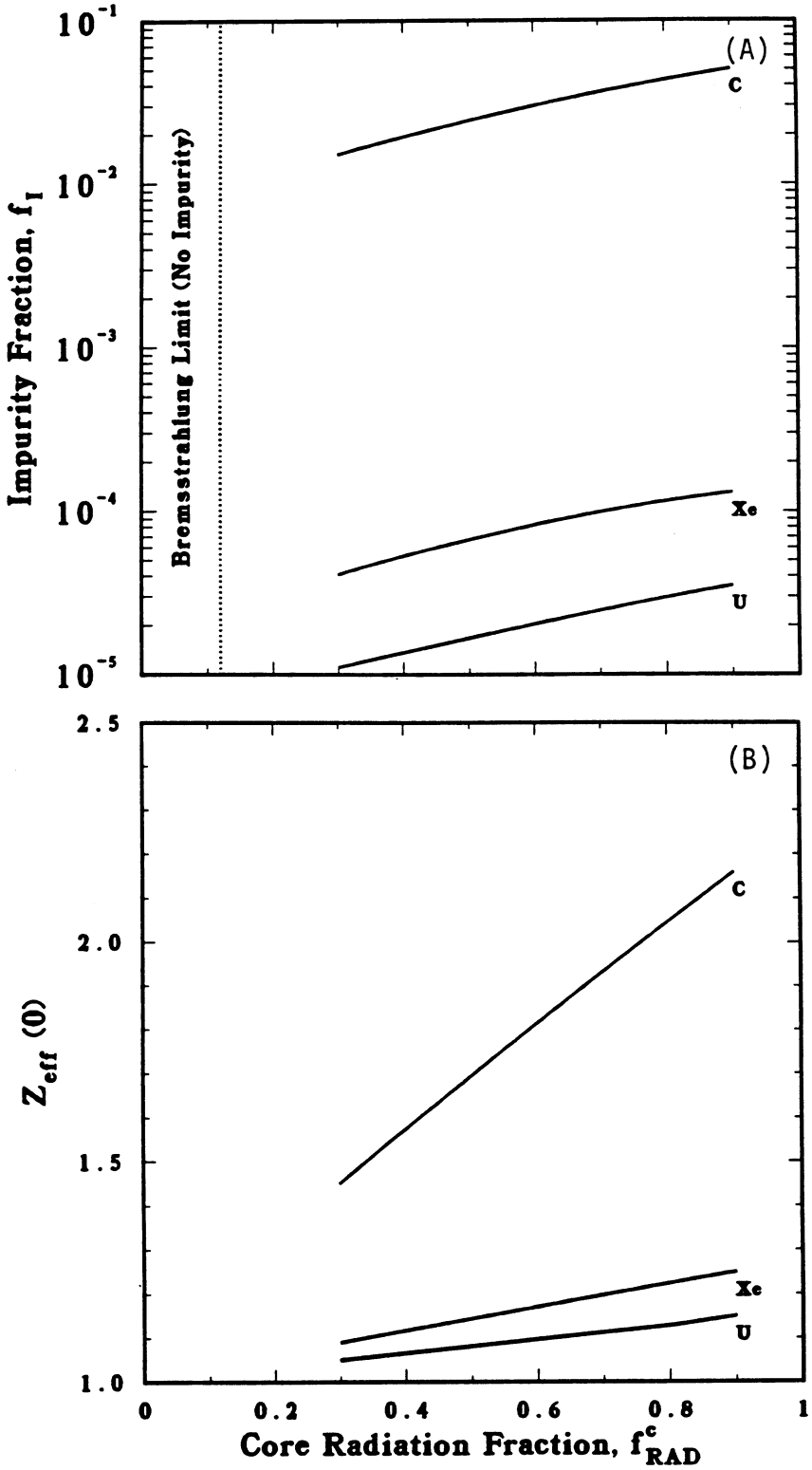

Figure 5.3-2. The required impurity fraction (A) and the resultant Z_{eff} (B) as functions of the core radiation fraction, f^c_{RAD}, for different impurities.

Table 5.3-IV.

IMPACT OF Xe IMPURITIES ON OHMIC DISSIPATION[a]

n_{Xe} (m^3)	f^c_{RAD}	T_i (keV)	T_e (keV)	Z_{eff}	g_{OHM}	P_{OHM} (MW)
2.9×10^{17}	0.77	10.6	9.6	1.67	4.88	46.6
0.	0.11	10.0	10.0	1.0	–	23.4
9.6×10^{17}	0.73	23.9	15.5	4.28	12.38	62.6
0.	0.11	20.0	20.0	1.0	–	8.0

[a] $\beta_\theta = 0.203$, $I_\phi = 17.9\,\mathrm{MA}$.

Listed below are the major unknowns associated with assuming β limits for RFP reactors. Even though a few of these issues may be partially addressed by 1-D analysis, the majority of the unresolved issues will require experimental demonstration at reactor conditions and, therefore, will remain unknown for some time.

- β-limited confinement scaling in the reactor plasma regime,
- Limit on the local β,
- The level and mechanism of the intrinsic transport,
- The collapse of the temperature profile due to impurity injection,
- The interaction of competing profile effects (*e.g.*, refueling, alpha-particle transport, $T_i : T_e : n$ split),
- The impact of the impurities on the edge plasma and the wall (*e.g.*, sputtering, wall buildup, vacuum, and tritium systems), and
- The effects of the impurities on the start-up transient.

Based on both experiment (Section 2.3) and theory (Section 2.2), it appears feasible that RFP reactors can exhibit a soft β limit. Such a β limit was assumed in choosing ZT-H experimental parameters [16]. If such β limits exist, it may be possible to adjust f^c_{RAD} to any level between 0.12 and 0.95, with only a minor increase (10% to 30%) in plasma resistance by injecting high-Z impurities into the plasma core. Only small variations in the impurity fraction are required to vary f^c_{RAD} significantly. In practice, the maximum operating value for f^c_{RAD} will be determined by the level of intrinsic transport. If the intrinsic transport mechanisms are classical, then the f^c_{RAD} upper limit could be higher than 0.99. Finally, it is noted that the impurity fraction of Xe required for $f^c_{RAD} = 1$ is two orders of magnitude smaller than that required for $f^c_{RAD} = 1$ in the divertor chamber.

5.3.3. Reference Design

Based on the 1-D analysis, the TITAN reference design is seeded with trace amount of Xe impurities ($n_{Xe} = 2.9 \times 10^{17}\,\mathrm{m}^{-3}$), resulting in a core radiation fraction, $f^c_{RAD} = 0.695$ and an overall $Z_{eff} = 1.68$. The computed equilibrium density and temperature profiles are shown in Figure 5.3-3. Analytical fits to these equilibrium profiles are:

$$\mu(r) = 2.843\left[1 - 0.44\left(\frac{r}{r_p}\right)^6 - 0.56\left(\frac{r}{r_p}\right)^8\right], \tag{5.3-9}$$

$$T_e(r) = \begin{cases} 14.40 - 46.94\left(\dfrac{r}{r_p}\right)^{2.8504} & \left(0. \;\; < \dfrac{r}{r_p} < 0.25\right) \\ 16.07 - 10.29\left(\dfrac{r}{r_p}\right) & \left(0.25 \; < \dfrac{r}{r_p} < 0.833\right) \\ 8.111 - 7.886\left(\dfrac{r}{r_p}\right)^{14.025} & \left(0.833 < \dfrac{r}{r_p} < 1\right) \end{cases}, \tag{5.3-10}$$

$$n(r) = 1.23 \times 10^{21}\left[1 - 0.8577\left(\frac{r}{r_p}\right)^{3.44}\right]. \tag{5.3-11}$$

The above analytical fits are plotted in Figure 5.2-1(B). The results of the 1-D code are compared in Table 5.3-V with the 0-D code results, and good agreement is found when the 0-D model uses density and temperature profiles that are similar to the 1-D results.

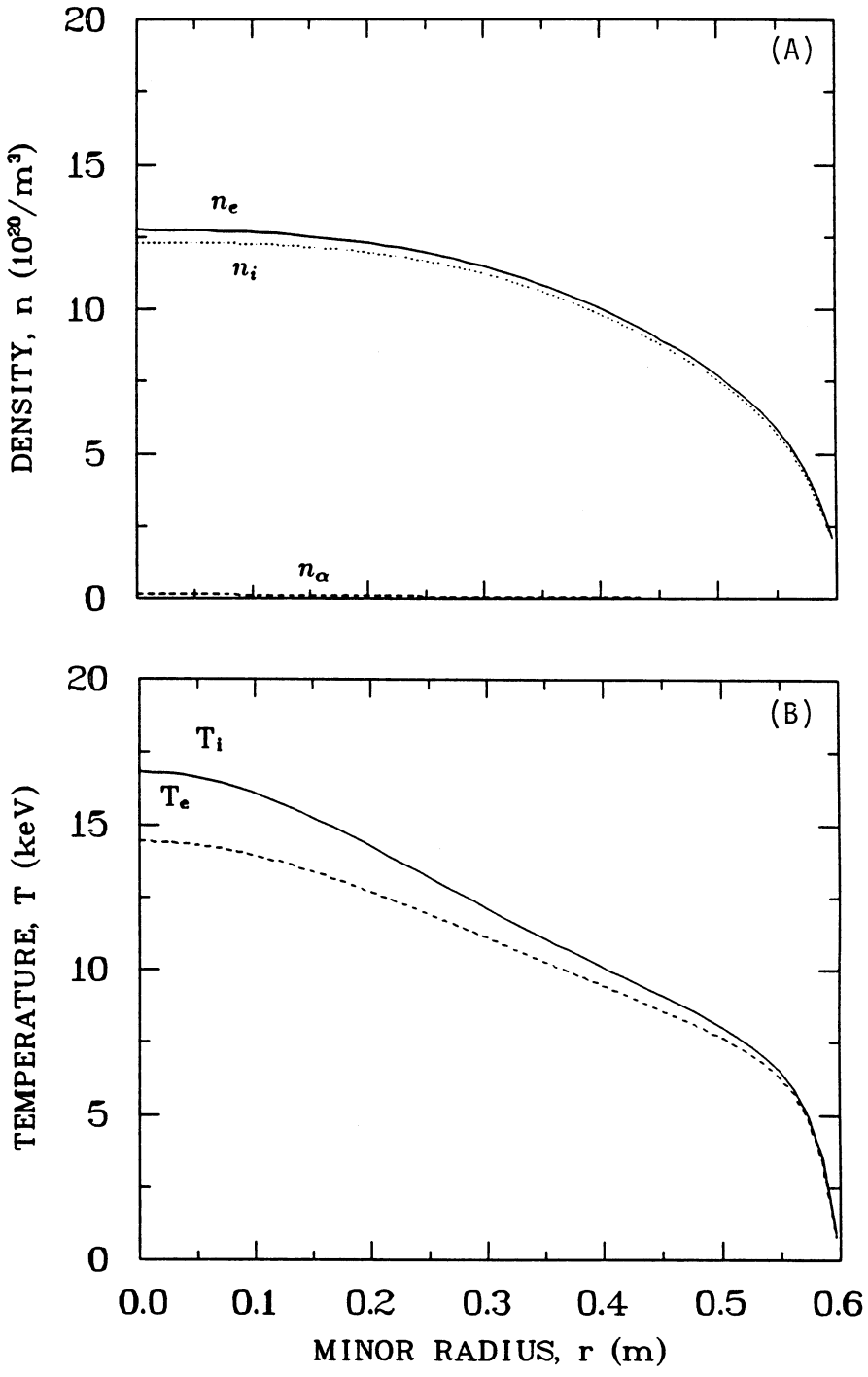

Figure 5.3-3. Profiles of plasma density (A) and electron temperature (B) from RFP-BURN.

Table 5.3-V.

COMPARISON OF 0-D AND 1-D PLASMA SIMULATION Of TITAN DESIGN POINT

Parameter	0-D	1-D
Minor plasma radius, r_p (m)	0.6	0.6
Major toroidal radius, R_T (m)	3.9	3.9
Average ion density, n_i ($10^{20}\,\mathrm{m}^{-3}$)	8.93	8.90
Density peaking, n_{io}/n_i	1.46	1.46
Alpha-particle fraction, n_α/n_i [(a)]	0.030	0.005
Ion temperature, T_i (keV)	10.0	10.8
Ion temperature peaking, T_{io}/T_i	1.46	1.56
Electron temperature, T_e (keV)	9.5	9.9
Electron temperature peaking, T_{eo}/T_e	1.46	1.46
Global particle-confinement time, τ_p (s)[(b)]	0.86	3.6
Global energy-confinement time, τ_E (s)	0.215[(c)]	0.20
Lawson parameter, $n_i\tau_E$ ($10^{20}\,\mathrm{s/m^3}$)	1.92	1.78
Poloidal beta, $\beta_\theta^{(d)}$	0.22[(e)]	0.207
Z_{eff}	1.69	1.68
Core plasma-radiation fraction, f_{rad}^c	N/A	0.695
Toroidal plasma current, I_ϕ (MA)	17.8	18.0
Ohmic power, P_{OHM} (MW)	28.5	28.1
Fusion power in plasma, P_F (MW)	2,301.	2,636.
Profile enhancement factors:		
DT reactivity, g_{DT}	1.40	1.32
Ohmic dissipation, g_{OHM}	2.92	2.72
Bremsstrahlung, g_{BR}	1.17	1.19

(*a*) Steady-state n_α depends upon $\tau_{p\alpha}$ assumption.

(*b*) $\tau_p \simeq 4\tau_E$ for 0-D and $\tau_p \simeq 4\tau_E/(1 - f_{RAD}^c)$ for 1-D.

(*c*) Based on the empirical scaling $\tau_{Ee} = C_\nu I_\phi^\nu r_p^2$ with $\nu \simeq 1$ and $C_\nu \simeq 0.05$ based on a fit to experimental data (Figure 2.3-20).

(*d*) At steady state, 2 to 3 times this $n\tau_E$ value is required for ignition.

(*e*) Including energetic alpha-particle pressure.

5.4. EDGE-PLASMA SIMULATIONS

The characteristics of the edge plasma have been of major importance in the TITAN design and extensive simulations of the edge plasma were undertaken. The main objectives of these simulations were to predict the plasma conditions at the first wall and divertor target and provide specifications for the engineering design of these components, and to estimate the requirements for particle removal. To obtain a self-consistent view of the behavior of the plasma and neutral particles, this analysis has been coupled to the modeling of the core plasma (Section 5.3) and the neutral particle transport (Section 5.5).

The design of in-vessel components (divertor plate, limiter, first wall) is a critical issue for all reactors and poses a particularly severe constraint for high-power-density reactors, such as TITAN. The key problem is to dispose of the steady-state plasma power (alpha-particle and ohmic) while maintaining acceptable heat fluxes and erosion rates on all components. In the scoping phase of the TITAN study [17], a simulation of the edge plasma without impurity radiation indicated plasma temperatures in the range $50 - 100\,\mathrm{eV}$ at the first wall, with very high heat fluxes on the divertor target. Attempts to reduce these loadings, by creating a region of localized radiation in the divertor, failed, as described more fully later, because of difficulties in preventing uncontrolled contamination of the core plasma by the injected impurities. The final proposed solution is to produce balanced radiation from the core plasma, the edge or scrape-off layer (SOL) plasma, and from the divertor plasma. The plasma is deliberately doped with a trace amount of a high-Z xenon impurities to create strong radiative cooling and spreading the heat load uniformly over the largest possible area (first wall). This high-radiation regime of operation, which appears to be an essential ingredient for a high-power-density reactor, may be more easily achieved in RFPs than in tokamaks because experimental evidence suggests that RFPs operate with a soft β limit. These issues are described in detail in Section 5.3.

Although two separate fusion-power-core designs were studied for the TITAN reactor, lithium-cooled for TITAN-I and an aqueous solution of a lithium salt as the coolant and breeder for TITAN-II, both designs had the same plasma parameters. Therefore, edge-plasma analysis was not duplicated and, although there are certain references specifically to the TITAN-I design, only minor modifications would be required for TITAN-II. A cross section of the outboard mid-plane of the TITAN-I divertor region is given in Figure 5.4-1, which shows the location of coils, divertor target, field lines, and the vacuum duct. This design represents the result of extensive iterations between edge-plasma and neutral transport analyses, magnetics design, and engineering design of the divertor target plate.

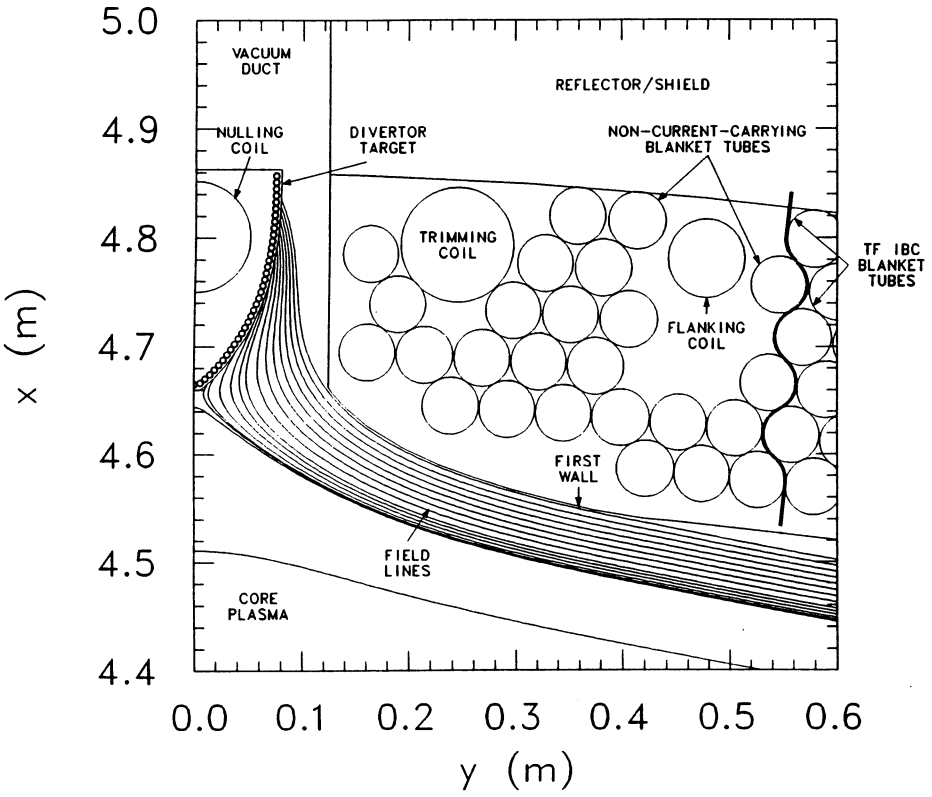

Figure 5.4-1. Outboard equatorial plane view of divertor section for TITAN-I.

5.4.1. Edge-Plasma Model

The edge-plasma analysis was carried out using the recently developed quasi-2-D transport code ODESSA [18,19]. The code retains the computational advantages of a 1-D radial transport code but incorporates important parallel physics. The localized nature of recycling at the divertor target allows two essential axial domains of interest, namely, the upstream or SOL zone and the downstream or recycling zone in the divertor (Figure 5.4-1) to be identified. By introducing suitable axial averaging operators, a set of coupled 1-D time-dependent equations for the plasma parameters in the SOL and divertor zones is obtained that incorporates explicit radial variation and essential parallel-transport processes, as well as the sheath condition. The 1-D nature of the code is a major design virtue computationally because extensive parametric studies are possible and necessary to achieve a converged design. A detailed description of the model and numerical approach is given in References [18] and [19]. Recent modifications to the model [20] are the addition of a self-consistent neutral-atom recycling model in the divertor chamber and a high-Z (xenon) impurity radiation model for radiative cooling at sub-200 eV temperatures.

The neutral density model is a simplified but reasonably accurate time-dependent model that assumes a radially flat neutral profile. However, the magnitude evolves self-consistently in time with changing plasma conditions in the divertor through temperature-dependent reaction rates and a prescribed pumping rate, which depends on such factors as geometry and pipe conductances. Prescribing the pumping time is believed to be more physical than the customary practice of fixing the recycling coefficient [21]. The recycling coefficient is then computed self-consistently from the relative amounts of ionization and leakage when the plasma reaches steady state. The flat profile assumption is justified on the grounds that charge-exchange-induced diffusion, which strongly dominates ionization at the low divertor temperatures encountered ($T_e \sim 5\,eV$), smooths spatial gradients of neutral density. This behavior is also seen in Monte Carlo simulations of neutral transport in the divertor.

In the absence of reliable data for the radiative cooling rate of high-Z elements at low plasma temperatures, a simple model is used to estimate the impurity radiation. Post has tabulated data for the radiative cooling rate in coronal equilibrium of many impurities in relatively high-temperature plasmas [22]. For xenon, these data are available only for temperatures above 80 eV and, therefore, have been extrapolated here for lower temperatures. Consideration of the electronic structure of xenon ions at these plasma temperatures suggests that, with reducing temperature, the cooling rate may increase somewhat before falling and finally drops to a very low value for temperatures below a few eV. To avoid introducing unwarranted complexity into the model, the cooling rate is assumed to remain constant with falling temperature, before falling to zero at the lowest temperatures. The model used for the radiative cooling rate as a function of plasma temperature, $L(T)$, of xenon impurities is

$$L(T) = L_0 \{1 - \exp[-(T/T_0)^n]\} , \qquad (5.4\text{-}1)$$

where L_0 is a constant (equal to $5 \times 10^{-12}\,eV\,m^3/s$), T_0 is taken as 10 eV, and a value of 2 was used for the exponent n. The rate of decay was varied to give a reasonable physical model that was not constant to zero temperature on the one hand, and that did not trigger thermal instabilities on the other hand. It is recognized that this model for the magnitude of the cooling rate is rather uncertain, not only because of the extrapolation to lower temperatures, but also because it is not clear that the assumption of coronal equilibrium itself is valid.

The impurity density profile was assumed radially uniform in the core and edge, and justified on the grounds that with an anticipated edge fueling of xenon, a flat profile was more reasonable than a constant fraction of the electron density. However, in the

divertor, recycling of the impurities is likely to drive the impurity concentration to some fraction of the electron density. This fraction was made consistent with the upstream concentration.

Transport coefficients used were similar to those utilized for 2-D simulations of the NET/INTOR tokamak designs [21]. There are few reports of the transport coefficients in the edge of RFP plasmas but, for large burning plasmas, it might be expected that they would be comparable to the values in tokamaks. The radial particle-diffusion coefficient was taken as $1\,m^2/s$ with a thermal diffusivity of $4\,m^2/s$. Boundary conditions at the first wall and divertor target were also standard [21,23]. Electron and ion temperature radial scale lengths at the first wall of 10 cm were assumed, with a zero density gradient. This latter assumption is necessary to prevent the loss of particles to the first wall, which will act as a perfect reflector in the steady-state plasma operation. A sheath boundary condition was imposed to model energy transmission at the divertor target.

An important difference from other edge-plasma simulations, however, was the treatment of the core/edge interface. In standard 2-D fluid simulations of edge plasmas [21,23], either fluxes of particles and heat from the core are prescribed at the separatrix, or the plasma density and temperatures are specified there. The core is thus assumed to be in steady state and not to respond to the dynamics of the SOL and divertor. This is a computational necessity since the iterative coupling of $1\frac{1}{2}$-D core-transport and 2-D edge-transport codes would be prohibitively expensive. However, ODESSA is not bound by the same computational restrictions and, thus, extensive iterations with the core transport code described in Section 5.3 were performed to ensure self-consistency at the core/edge boundary of heat and particle fluxes, and of plasma density and temperatures.

The simplified neutral model in ODESSA was introduced to avoid having to complement the plasma evolution with detailed neutral-source distributions from Monte Carlo calculations at every time step. Although the model is adequate for the description of recycling in ODESSA, it does not provide estimates of leakage of neutral atoms and molecules across the separatrix back to the main plasma, or relative fluxes of D, T, and He that are pumped. It also cannot address the question of He enrichment at the pumps. For these reasons, the plasma computations were supplemented with 3-D Monte Carlo neutral-transport simulations in the relevant TITAN divertor geometry, using the DEGAS code [24] (Section 5.5).

5.4.2. Edge-Plasma Parameters

Detailed field-line tracing calculations (Section 4.4) show the field-line connection length, $L_{||}$ (defined as the distance along the field line from the "watershed"point between divertors to the target), to be sensitive to the distance into the SOL, especially in the vicinity of the separatrix. However, since the resolution on transport scales is at best an island width, a suitable average over the SOL width was taken for the ODESSA simulations, at a value $L_{||} = 69\,\mathrm{m}$.

After considerable iteration between core- and edge-plasma models, as well as thermal and mechanical design of the divertor and magnetics analysis, the converged and optimum design consists of three divertors and an SOL width of 6 cm. The choice of the number of divertors was a compromise between conflicting desires. As the number of divertors increases, the total area of the divertor targets increases, leading to a lower heat flux (as shown in Section 5.4.3), but the ohmic losses in the lithium divertor coils also increase. The choice of SOL width was also a trade-off; a small SOL thickness is desirable for reasons of plasma MHD stability, but it leads to higher plasma temperatures at the first wall and a consequent increase in erosion.

In the final converged stage between core- and edge-plasma codes, stable profiles of plasma density, temperature, and flow velocity in the SOL and divertor were obtained for $\sim 150\,\mathrm{MW}$ of power flowing into the SOL at a particle throughput of $\sim 10^{22}\,\mathrm{s}^{-1}$. In the global-plasma power balance, $\sim 70\%$ of the steady-state heating power was radiated in the core plasma, $\sim 23\%$ in the SOL, 4% in the recycling zone, and 3% was deposited on the target through the plasma sheath.

Figure 5.4-2 depicts the radial upstream and downstream ion and electron temperature and density profiles. High separatrix density ($\sim 2 \times 10^{20}\,\mathrm{m}^{-3}$) and temperatures ($T_e \sim 220\,\mathrm{eV}$, $T_i \sim 380\,\mathrm{eV}$) are achieved, with the latter decaying strongly to $\sim 2\,\mathrm{eV}$ at the first wall. This is largely due to the intense radiative cooling and strong rethermalization between ions and electrons near the first wall. Near the separatrix, however, strong parallel-electron conduction results in a depressed electron-temperature profile at that location compared with that of the ions. The density profile, on the other hand, is quite flat, partly as a consequence of the assumed first-wall reflection coefficient of unity, but also because of the unusual flow pattern (see below) that results in a very weak net flow into the divertor.

Intense recycling (global recycling coefficient, $R = 0.995$) is achieved at the divertor target based on the simple neutral-particle model in ODESSA, which, as discussed in

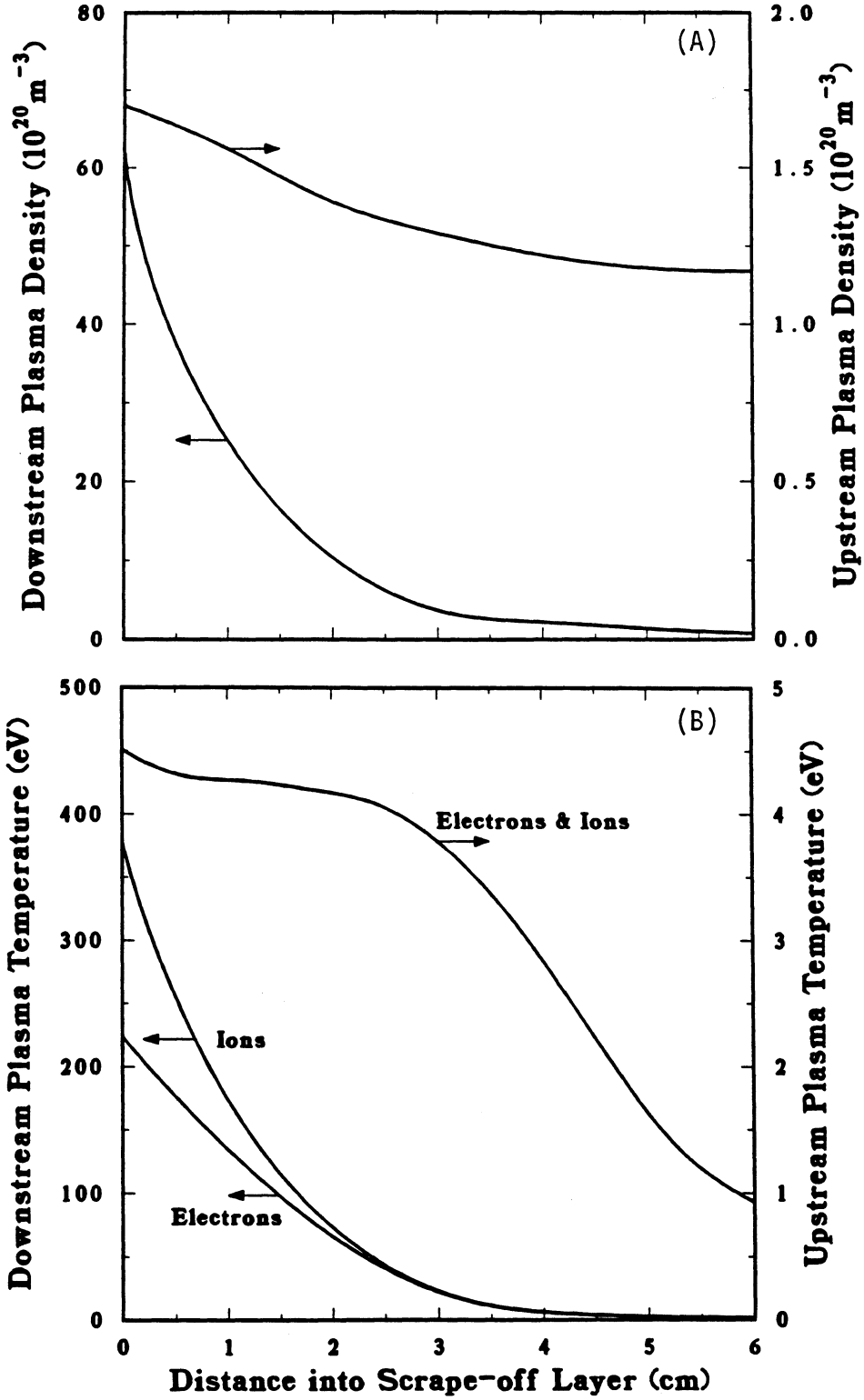

Figure 5.4-2. Radial profiles of plasma temperature (A) and density (B), in upstream (SOL) and downstream (divertor) zones.

Section 5.5, is borne out by more detailed Monte Carlo simulations. This is characterized by high density ($\sim 10^{21}\,\mathrm{m}^{-3}$) and low temperature ($T_e \simeq T_i \simeq 5\,\mathrm{eV}$) in the divertor plasma. Because the cross section for electron-impact ionization is sensitive to the electron temperature, the ionization rate is greater near the separatrix than in the cooler regions near the first wall (most of the energy here is radiated upstream). As discussed in Section 5.5, the low temperature achieved is a significant factor in permitting a viable first wall and divertor design from an erosion viewpoint.

Figure 5.4-3 shows the radial profile of the upstream flow velocity towards the divertor. A striking observation is that the flow is reversed in the vicinity of the separatrix and accelerates to nearly sonic flow at the first wall. This complex flow pattern is a consequence of intense recycling in the divertor that causes the *local* recycling coefficient to exceed unity at certain locations. This in turn induces the axial pressure profile to invert, resulting in particles being driven *out* of the divertor there. A detailed explanation of this phenomenon, which describes the complex dependence on the T_e profile, has been published elsewhere [25]. A diffusive/convective circulation is thus set up between the SOL and divertor. This effect occurs independently of the radiation in the edge, but it rules any attempt to localize all radiative cooling to the divertor plasma because impurities could not be confined exclusively to that region. For this reason, the decision was made to allow radiation uniformly in the plasma.

5.4.3. Sensitivity Study

In view of the considerable uncertainty in many of the assumptions used in the edge-plasma analysis, an extensive sensitivity study was undertaken in an effort to determine how the divertor design might change as the edge-plasma conditions change. For each different value used for an input parameter, the ODESSA code was rerun. Although it was too time-consuming to iterate with the core-plasma code for each case studied, the variations about the central values were sufficiently small that the results would not be greatly different for a fully converged solution. Since every output parameter (*e.g.*, plasma temperatures, densities, heat fluxes, *etc.*) is different for each variation, it would be impractical to examine the effect of changes on each parameter of interest. Because the divertor-target heat flux has been the critical issue for the TITAN divertor design, this factor has been emphasized in the sensitivity study. Further, to reduce the focus of attention to a single value, the heat flux has been averaged across the target, as adjustments in the shaping of the target could be made to smooth out sharp peaks in the loading.

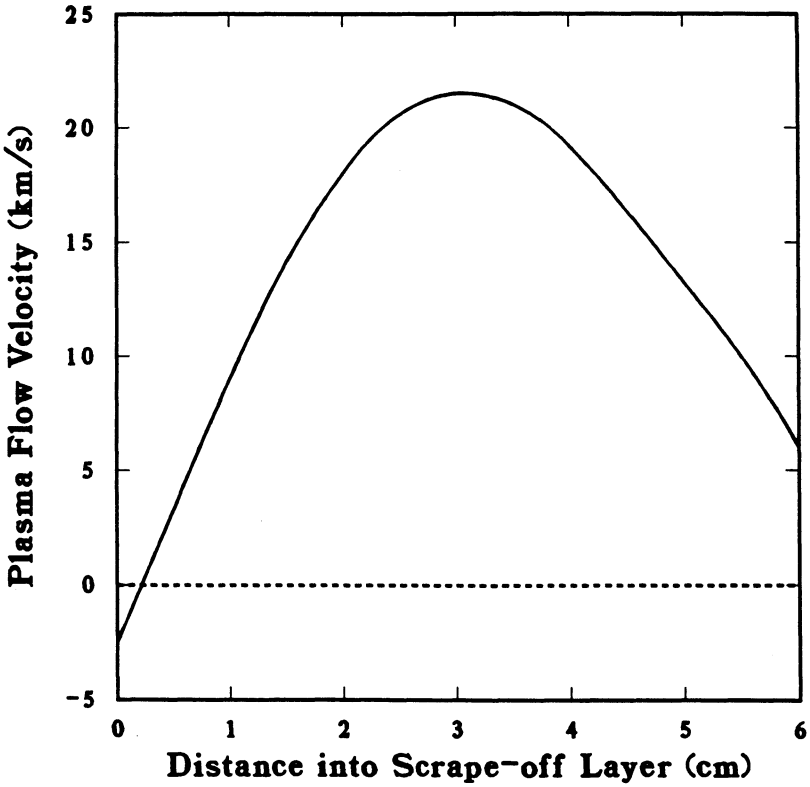

Figure 5.4-3. Radial profile of plasma flow velocity in upstream (SOL) zone.

Variations were considered in the following parameters: radial particle-diffusion coefficient, $D_\perp$; ratio of thermal-to-particle diffusivities, $\chi_\perp/D_\perp$; neutral-particle pumping time, τ_{pump}; constants in the impurity model, L_0 and T_0; field-line connection length, $L_\parallel$; scrape-off layer thickness, Δ_{SOL}; core plasma-radiation fraction, f^c_{RAD}; and the number of divertors, N_D. The results of this study are given in Table 5.4-I, giving the average divertor-target heat flux, q''_D. Note that this heat flux is strictly for TITAN-I, but the trends in the data would exist for TITAN-II.

Fairly substantial changes (factor 2–3) in the transport coefficients and in the neutral pumping time lead to relatively small changes in the heat flux on the divertor target of less than 10% to 12%. Note that the profile of heat flux in the plasma may vary quite noticeably, particularly as the transport coefficients are adjusted, but the total power flow to the target (or, equivalently, the average heat flux) is less sensitive. The results are somewhat more sensitive to the parameters in the impurity radiation model, since 20% changes in the input variables yield changes in the heat flux of up to 10%. The connection length makes little difference to the heat flux (verifying that including a different value for each field line is not important), and there is also little sensitivity to the

Table 5.4-I.

SENSITIVITY STUDY FOR EDGE-PLASMA ANALYSIS

Variable	Reference Value	New Value	q''_D (MW/m^2)	Percent Change
Reference case			6.8	
$D_\perp$ (m^2/s)	1.0	0.5	7.6	+11.9
		2.0	6.1	−11.3
$\chi_\perp/D_\perp$	4.0	2.0	7.3	+7.2
		6.0	6.5	−4.4
τ_{pump} (ms)	0.3	0.1	7.2	+5.9
		1.0	6.6	−3.2
L_0 (10^{-12} eV m^3/s)	5.0	4.0	7.5	+9.7
		6.0	6.4	−6.6
T_0 (eV)	10.	8.0	7.3	+7.2
		12.0	6.5	−4.8
$L_\parallel$ (m)	69.	64.	7.0	+3.1
		74.	6.7	−2.5
Δ_{SOL} (cm)	6.0	5.0	6.7	−2.1
		7.0	7.0	+2.1
f^c_{RAD}	0.70	0.65	7.9	+16.0
		0.80	5.0	−27.0
N_D	3	2	8.0	+16.9
		4	6.2	−9.2

SOL thickness. The strongest sensitivity occurs with the core plasma-radiation fraction, where the average heat flux varies approximately as $(1 - f^c_{RAD})^{-1}$. This sensitivity could be utilized to adjust for any uncertainties in other parameters (especially the radiation model, which is probably the weakest aspect of the model) by varying the impurity density to ensure that the heat flux on the divertor is acceptable. Finally, the sensitivity of the heat flux to the number of divertors is weaker than the expected $1/N_D$ dependence, which is explained by the following observations: For an increased number of divertors, the connection length is reduced, leading to less radial diffusion and a lower average density in the SOL. The impurity radiation is therefore reduced and more power is deposited on the divertor target.

5.5. NEUTRAL TRANSPORT AND EROSION

5.5.1. Neutral Transport Calculations

This section describes the modeling of neutral particle transport that was performed for the TITAN divertor design. The actual geometry modeled was based on the TITAN-I divertor and vacuum-system designs, but the general trends of the results are also valid for TITAN-II. The reason for undertaking detailed neutral-transport simulations was to ensure that the simplified neutral model incorporated in the ODESSA edge-plasma modeling (Section 5.3) adequately predicted the recycling and particle removal in the divertor. Further, certain aspects of the modeling can only be carried out with a full neutral-particle model; for example, the question of whether the open divertor geometry used in TITAN, and the consequent proximity of the divertor target to the core plasma, leads to an unacceptable leakage of neutral particles from the divertor across the separatrix.

The detailed neutral-transport modeling was provided by DEGAS, a fully 3-D Monte Carlo transport code [24], which uses the most recent and thorough data base of cross sections and reflection coefficients.

The geometry of the TITAN-I toroidal-field divertor was modeled using an equatorial-plane cross section of the divertor plasma and duct region. This planar section was then rotated about the plasma centerline to obtain the poloidally continuous divertor chamber. The divertor cross section actually varies continuously with poloidal angle, because of the variation of toroidal field with major radius, but the computational effort required for a nonsymmetric 3-D model was considered excessive. Therefore, both outboard and

inboard geometries were examined (each with an assumed poloidal symmetry) in an effort to bound the result.

The duct leading from the divertor to the vacuum tank is not poloidally continuous and is located over the outboard 90° in poloidal angle only. This feature is modeled by specifying this surface to be an absorbing wall over this angle, and to be solid over the remaining 270°.

The outboard cross-section geometry is shown in Figure 5.4-1 in relation to the divertor coils and blanket. In Figure 5.5-1, the grid representing this area in DEGAS is shown with a single particle trajectory. As this particular particle was launched from an inboard zone, the outermost boundary is a wall, rather than a pumping duct. In this case, the particle bounces off the walls in the duct for a long time until it either returns to the plasma and is re-ionized or it eventually finds its way around poloidally to the exit duct.

The plasma conditions that are required as an input to the code are taken from the edge-plasma code ODESSA. Since the axial (*i.e.*, along the field line) variation of

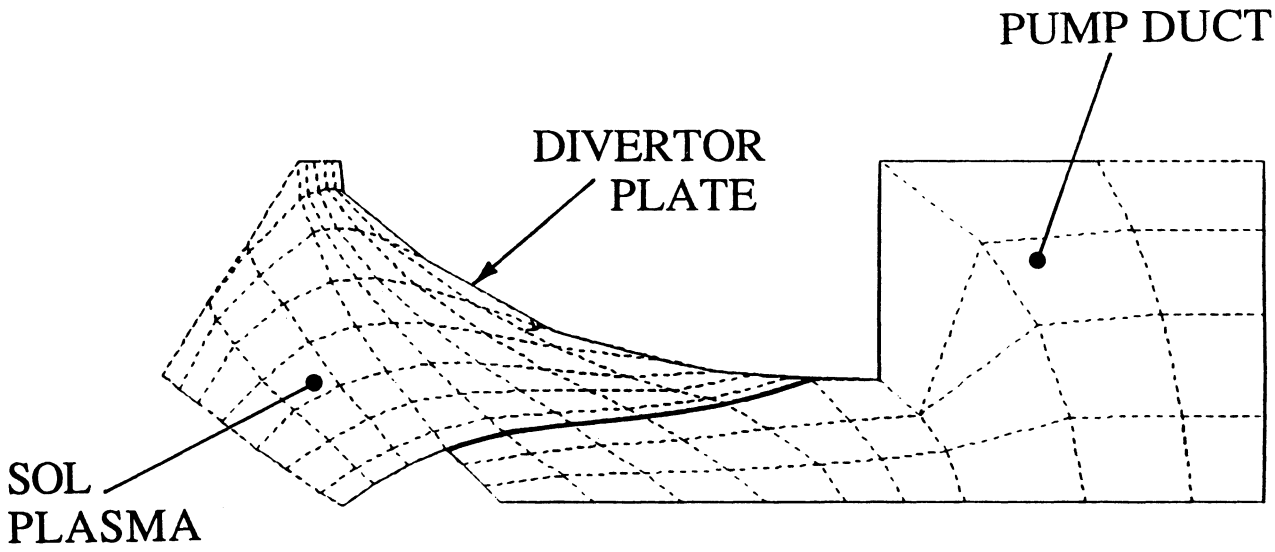

Figure 5.5-1. Mesh used for neutral particle modeling with DEGAS code, showing a typical particle trajectory.

the plasma parameters is needed but ODESSA provides only values at only two axial locations, a linear interpolation is made between the downstream values that apply at the divertor target, and the upstream values that are taken as applying at a set of radial points passing through the null point. Further upstream, the plasma parameters are assumed to be constant. Magnetic flux expansion at the target is also accounted for in computing the particle flux and neutral source at the target.

Figures 5.5-2 and 5.5-3 show the poloidally averaged neutral-particle density for, respectively, the species atomic D and molecular DD, and for He for the outboard divertor geometry. Going upstream in the plasma away from the divertor target and in the SOL near the separatrix, the neutral densities fall very sharply so that the flux of neutral particles across the separatrix and into the core plasma is negligible. The lack of any significant leakage into the core plasma arises from the high plasma density ($\sim 10^{21}\ \mathrm{m}^{-3}$) near the divertor target, which leads to the neutrals emitted from the target having a short mean free path to ionization. Therefore, despite the closeness of the divertor target to the core plasma, the proposed configuration acts as a divertor rather than as a limiter.

Further upstream from the target, in the SOL area near the first wall, the neutral particle density falls off much more slowly giving rise to a neutral channeling effect between the first wall and the higher density and warmer (*i.e.,* more ionizing) plasma nearer the separatrix.

The densities are high in the duct region and, for atomic D, fairly constant throughout the duct region, with pressures of about 15 to 75 mtorr depending on the poloidal location; the poloidal asymmetry in the pressures is discussed later. These high pressure values pose a qualification on the assumption used in the neutral transport model that the neutrals are in the free streaming regime, in which case neutral-neutral collisions can be neglected. This assumption is poor at these high pressures.

It is noted that there is little margin for movement of the separatrix position with respect to the target, and the possible movement due to the proposed oscillating-field current drive or other sources of fluctuations is not known. An additional point is that the results apply to the full-power operating state and the transient conditions during start-up were not addressed with respect to this issue. Consideration must be given to these transient conditions so that a period of low plasma density does not coincide with a period of relatively high divertor power. This combination can give rise to an excessive interaction between the divertor target and the core plasma, as well as the possibility of high plasma temperatures at the divertor target and the resultant problem of sputtering damage. Fueling in the divertor may help to alleviate these undesirable conditions.

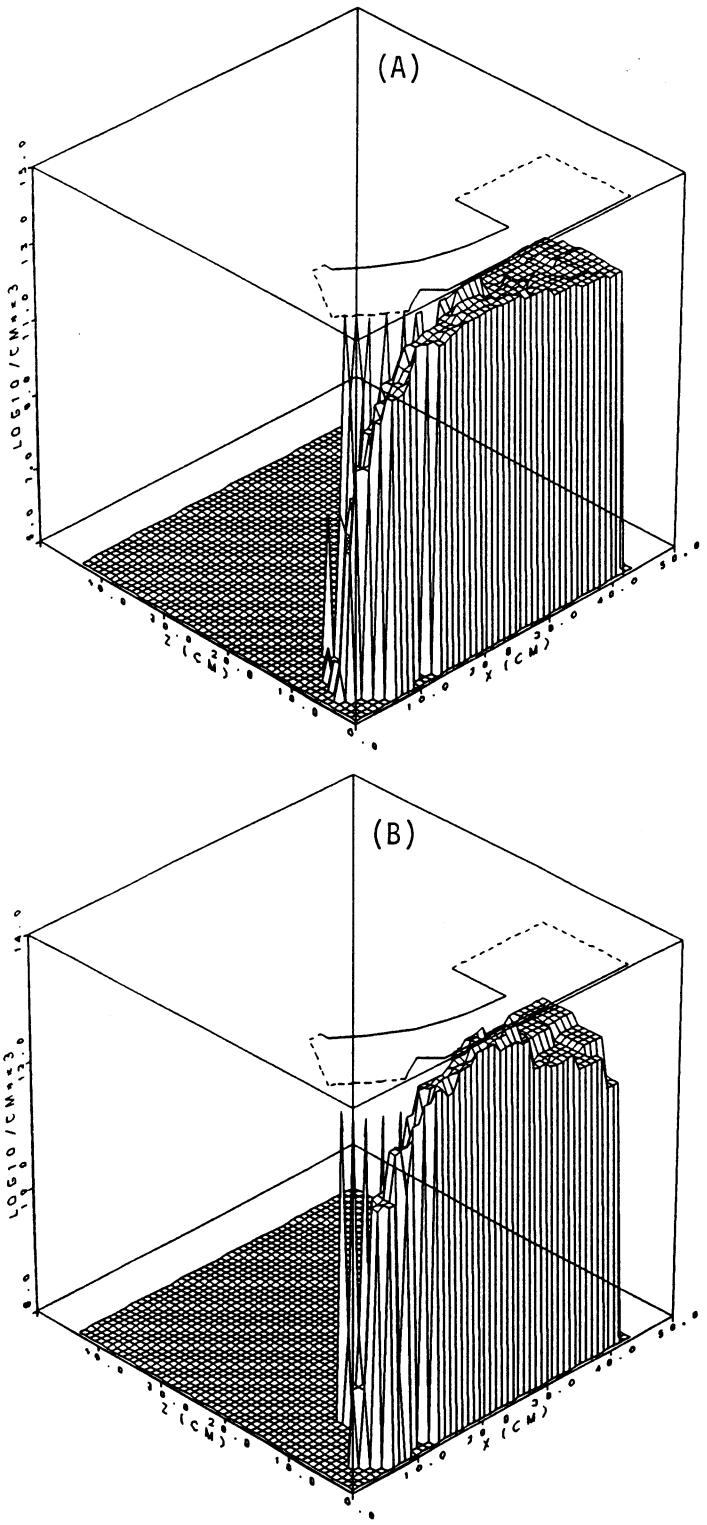

Figure 5.5-2. Poloidally averaged density of atomic D (A) and molecular DD (B) for TITAN-I divertor geometry.

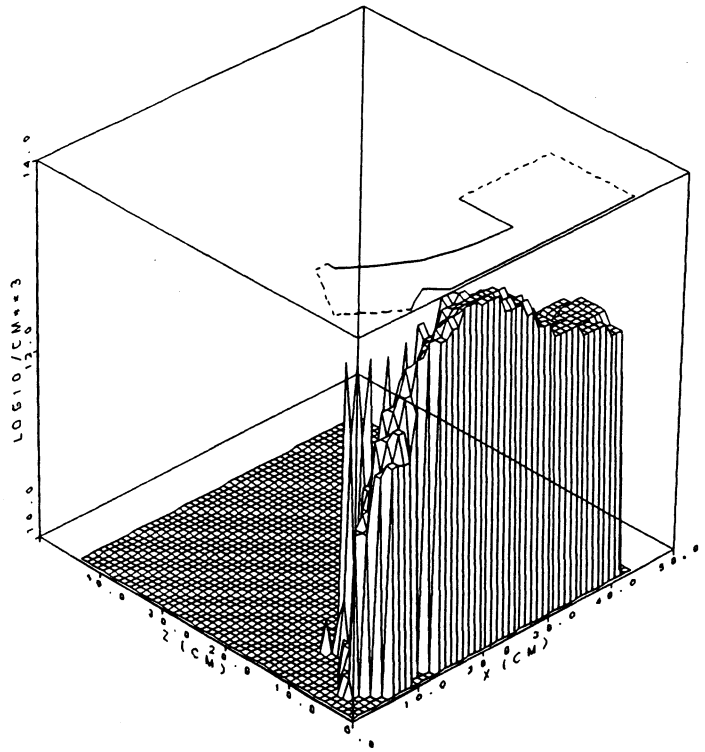

Figure 5.5-3. Poloidally averaged density of He for TITAN-I divertor geometry.

The neutral transport results show that the global recycling coefficient, R, lies in the range 0.95 to 0.98, depending on the geometry and plasma specifics; the corresponding value predicted by the ODESSA edge-plasma code is 0.995. This slight mismatch in recycling coefficients exists because the codes have not been iterated to convergence. To achieve the higher recycling desirable for optimum divertor operation, it may be necessary to make minor adjustments to the divertor duct geometry to increase the fraction of neutrals that are reflected back into the plasma and re-ionized.

The radial profile of plasma flow velocity upstream of the recycling zone can be evaluated by integrating the ionization source term along the field line away from the target, and ignoring cross-field transport. This analysis indicates that the flow should reverse, as discussed in Section 5.3 and Reference [25]. However, the DEGAS results imply that the reversal will occur on field lines near the center of the SOL, in contrast to the ODESSA results where reversal occurs near the separatrix. Iteration between the two codes, particularly in the areas of radial neutral-particle profiles, would remove this discrepancy.

The fluxes of neutral particles escaping into the pumping duct were found to be significantly different from the plasma fluxes on the divertor target, specifically the neutral

gas was enriched in D and He relative to T. For the assumed case of equal target fluxes of D and T, and for an He plasma flux of 5% that of DT, the neutral gas escaping was enriched in He relative to DT by a factor of ~ 3 and in D relative to T by a factor of 3.7.

The enrichment of He in the neutral exhaust, which has been observed in other simulations (*e.g.,* Reference [26]), improves the ash pumping efficiency and this benefit has been included in the specifications for the vacuum system design. The enrichment arises from the smaller cross sections for charge exchange and for ionization of He relative to DT, which lead to a longer mean free path and an increased probability of escape from the plasma.

Enrichment of the pumped gas in D relative to T appears to be a new result and is due to the mass difference between the two isotopes. The probability, p, of escape of a neutral from the divertor plasma can be approximated as $\exp(\Delta/\lambda)$, where Δ is the average path length of a neutral from the target through the plasma, and λ is its mean free path. If Δ is taken as 0.1 m, a reasonable estimate for the TITAN geometry, then for the average plasma density of $2 \times 10^{21}\,\mathrm{m}^{-3}$ and a plasma temperature of 4 eV, the enrichment ratio of D relative to T is estimated to be about 3, in reasonable agreement with the DEGAS results. Although a more extensive study of this effect is necessary, the apparent de-enrichment in tritium reduces the tritium throughput in the gas handling systems which is an important benefit.

The neutral particle pressure shows a marked asymmetry in poloidal angle because of the presence of the pumping duct only on the outboard side of the divertor. For atomic D, the pressure on the outboard side of ~ 15 mtorr is less than the inboard pressure by a factor of 4 to 5, because the outboard duct acts as a particle sink. The asymmetry is even larger for DD where the inboard pressure is about 10 times more than that of the outboard. For this case, the source of DD is neutrals emitted from the chamber walls with the wall area being larger on the inboard side. Thus, the source, as well as the sink, is poloidally asymmetric and so the pressure differential is increased for DD over that for atomic D.

The neutral particle density within the plasma region, especially that of atomic D, however, is largely constant with poloidal angle. There is an asymmetry (about a factor of 2 greater inboard than out) in the density of molecular DD in the low plasma-density region of the SOL, but the plasma density source is dominated by the atomic D species. These observations show that the assumption that the plasma conditions retain a poloidal symmetry while the neutral particle pressure in the duct is poloidally asymmetric is justified.

5.5.2. First Wall Erosion

The DEGAS neutral-transport code was used to estimate erosion on the first wall of TITAN; the wall material chosen was vanadium (TITAN-I) but the results should be similar for the ferritic steel proposed for TITAN-II. Sputtering due to both ions and charge-exchange (C-X) neutrals was considered, using the upstream plasma profiles provided by ODESSA. The wall flux could not be taken directly from the results because a flat density profile was assumed as a wall boundary condition to conserve particles. Therefore, the DT ion flux on the wall was estimated at $2 \times 10^{21}\,\mathrm{m^{-2}s^{-1}}$, with a 5% He ion fraction, from an approximate model of recycling at the first wall.

The reference case of the ODESSA model predicts a plasma temperature (ion and electron) of slightly less than 2 eV at the first wall. This implies negligible ion erosion since the ion energies are below the threshold for sputtering. Further, the high plasma density near the first wall prevents the neutral particles released from the wall from penetrating to regions of high plasma temperature and then returning to the wall to pose a sputtering problem. However, the edge-plasma models contain a fairly large degree of uncertainty and, therefore, a sensitivity study was performed to estimate the erosion rate for different values of the plasma temperature at the first wall. Because it is not clear whether a sheath will form at the wall, cases with and without the presence of a negative sheath were considered. Table 5.5-I shows the results of this analysis in which redeposition was ignored.

As the engineering design of the first wall provides for a 0.25-mm allowance for erosion, these results imply that a plasma temperature of ~ 6 eV is acceptable if a sheath exists at the wall, while the temperature is allowed to rise to $\sim 10 - 20$ eV if there is no sheath; the limits would be increased further if redeposition were taken into account. ODESSA predicts a temperature of ≤ 2 eV so it appears that there is a large safety margin in the first wall design from considerations of erosion.

5.5.3. Divertor Plate Erosion

Erosion of the divertor target was calculated from the DT and He ion fluxes, allowing for acceleration through the plasma sheath. The location chosen for the calculation was a point close to where the separatrix strikes the divertor target, where the particle flux and temperature have their highest values. Allowing for magnetic flux expansion and the inclination of the target to the field lines, the DT ion flux is estimated to be $\sim 9 \times 10^{23}\,\mathrm{m^{-2}s^{-1}}$; the He ion flux is taken as 5% of this value. The first material

Table 5.5-I.

SENSITIVITY STUDY FOR FIRST-WALL EROSION RATE[(a)]

First Wall Temperature (eV)	DT Ions	DT C-X Neutrals	He Ions	Total
1.7	0.00 (0.00)	0.01 (0.01)	0.00 (0.00)	0.01 (0.01)
6.0	0.00 (0.03)	0.01 (0.01)	0.00 (0.25)	0.01 (0.29)
10.0	0.02 (1.02)	0.02 (0.02)	0.02 (0.78)	0.06 (1.82)
20.0	0.75	0.09	0.22	1.06
30.0	2.55	0.21	0.54	3.30

(*a*) Erosion rate in mm/y without (with) a sheath.

considered was vanadium (TITAN-I first-wall material) but the sputtering due to He bombardment was found to be excessive ($\sim 5 - 10\,\mathrm{mm/y}$) even at the low plasma temperature of 4 eV. It was concluded, therefore, that a high atomic number (Z) armor would be required to protect the cooled divertor plate; tungsten (alloyed with rhenium to improve its ductility) became the final choice (Sections 11 and 17).

Helium and DT sputtering on tungsten are negligible for the TITAN divertor plasma conditions. Based on considerations of the expected concentration of xenon impurities in the divertor plasma, the total Xe flux onto the target was estimated at $\sim 10^{20}\,\mathrm{m^{-2}s^{-1}}$. Many uncertainties exist regarding the behavior of the recycling Xe impurity, especially with respect to the flow speed and charge state when it strikes the target. There is a tendency for the impurity to be frictionally accelerated by the drifting background plasma such that it can be flowing at close to the sonic velocity of the DT ions. However, the mean free path for ionization of the neutral Xe atoms emitted from the target is short at these high plasma densities and there is little distance for the impurity to be accelerated to a high velocity before returning to the target. As an example calculation, it was assumed that the recycling Xe has a flow speed of one-tenth that of the DT plasma ions, but that the primary Xe flux has the same flow speed as the background plasma. If these species have charge states of, respectively, 2 and 4, then the erosion rate is

less than 2 mm/y even if redeposition is ignored. However, strong redeposition would be expected at the high plasma density found near the divertor target and may dominate the net erosion rate, implying that higher charge states and flow speeds could be tolerated. Acknowledging the great uncertainties regarding erosion estimates for the divertor target, the specification for the divertor design was that a 2-mm-thick layer of tungsten should be provided to give a lifetime of one full-power year. Further investigations into the effects of heavy impurities on the erosion rate of divertor targets clearly are required.

Significant erosion can occur on the wall facing the divertor plate from charge-exchange neutrals originating from the divertor target. Orientation of this wall at a relatively oblique angle to the target can reduce this erosion but it may be necessary to protect this surface with a thin layer of an armor material such as tungsten. Since this region of the wall is shadowed from the core plasma and receives a small heat load, this protection should not lead to thermal problems in the structure.

5.6. FUELING

The TITAN-I external fueling rate balances the combined DT exhaust and fusion burnup in steady state. The rate of generation and, hence, removal of helium ash by the fusion reactor is given by

$$\phi_{He} = \frac{P_F}{17.6 k_B}, \tag{5.6-1}$$

which for $P_F = 2{,}300\,\mathrm{MW}$ and $k_B = 1.602 \times 10^{-19}\,J/eV$ equals $\phi_{He} = 8.16 \times 10^{20}\,\mathrm{He/s}$ or $3.07\,\mathrm{Pa\ m^3/s}$ (23.4 torr l/s). The TITAN-I tritium burnup is 0.353 kg/d at a fractional burnup is 0.24, such that the tritium throughput rate is 1.5 kg/d. The performance of TITAN-II is similar. Assuming that the confinement times of deuterium and tritium in the plasma are equal ($\tau_{pi} \simeq 3.6\,\mathrm{s}$), the fueling stream can maintain the nominal composition of the plasma (including Xe impurities), subject to isotopic separation and removal of the alpha-particle ash.

Edge refueling is presumed to be inappropriate in TITAN because particles introduced at the first wall will tend to be swept out along the magnetic-divertor scrape-off (outside the separatrix) to the divertor plate and vacuum ducts and, therefore, will be unavailable to refuel the core plasma. Pellet fueling [27,28] using cryogenic pellets ($\rho_o \simeq 250\,\mathrm{kg/m^3}$) is the fueling option of choice. The RFP plasma confinement is provided largely near the reversal surface ($r_r \simeq 0.55\,\mathrm{m}$ for TITAN with $r_p = 0.60\,\mathrm{m}$), with turbulent mixing

of particles assumed to occur within the core plasma. It is assumed, therefore, that the pellet inventory needs to be deposited mostly just inside the reversal surface. Deep penetration to the central plasma is not required in an RFP, such that ultra-high pellet injection speeds ($> 3\,\mathrm{km/s}$) or advanced acceleration technologies [29] beyond the presently available pneumatic or centrifugal approaches [28], should not be required in the TITAN case.

The pellet ablation process has been considered by several authors [27,30 - 32]. The simple model applied here is the so-called "neutral-ablation-cloud" model [30]. Corrections for the perturbation of the local magnetic field by the pellet lead to somewhat (up to $\sim 50\%$) reduced pellet-ablation rates and longer lifetimes [31]. The surface ablation (not including alpha-particle effects) of a spherical pellet with initial radius a (m) is represented by the following expression [30] for the time-rate-of-change of the pellet radius:

$$\frac{da}{dt} = -1.0 \times 10^{-8} \frac{n_e^{1/3} T_e^{5/3}}{a^{2/3} m^{1/3}}, \tag{5.6-2}$$

where m (amu) is the molecular weight of the fuel (*e.g.*, 5 amu for DT), n_e (m^{-3}) is the target-plasma electron density, and T_e (keV) is the target-plasma electron temperature. Integration of Equation 5.6-2 gives the pellet lifetime, t_p (s), or the time after initial injection ($t = 0$) at which the pellet completely evaporates ($a \rightarrow 0$). Assuming a constant pellet injection speed, u (m/s), the maximum pellet-penetration distance, d (m), is given by $d = ut_p$. The integration of Equation 5.6-2 can be rewritten in the following form

$$\frac{3}{5} a^{5/3} = \int_s^{r_p} \frac{1.0 \times 10^{-8} n_e^{1/3}(r)\, T_e^{5/3}(r)}{m_i^{1/3} \mu}\, ds, \tag{5.6-3}$$

where $s = r_p - d$ is the penetration distance along a perpendicular injection trajectory aimed toward the plasma center ($r = 0$). Asymmetric pellet-surface ablation and consequent deflection of the pellet trajectory has been observed on the ZT-40M experiment [33] but is ignored in this model. The TITAN radial profiles of electron temperature, $T_e(r)$, and density, $n_e(r)$, are illustrated in Figure 5.6-1, and represent the profiles obtained by the 1-D plasma simulations fitted by, respectively, Equations 5.3-10 and 5.3-11.

Ablation of the pellet while traversing the scrape-off region between the first wall and separatrix is typically small but included in the present calculation. Ablation of the pellet, as the pellet penetrates the plasma, contributes to the local plasma particle inventory. The model assumes that the radial plasma-transport time ($\tau_D \simeq 20\,\mathrm{ms}$) is much longer than the parallel-transport time ($\tau_{\|} \simeq 240\,\mu\mathrm{s}$), which in turn is much longer

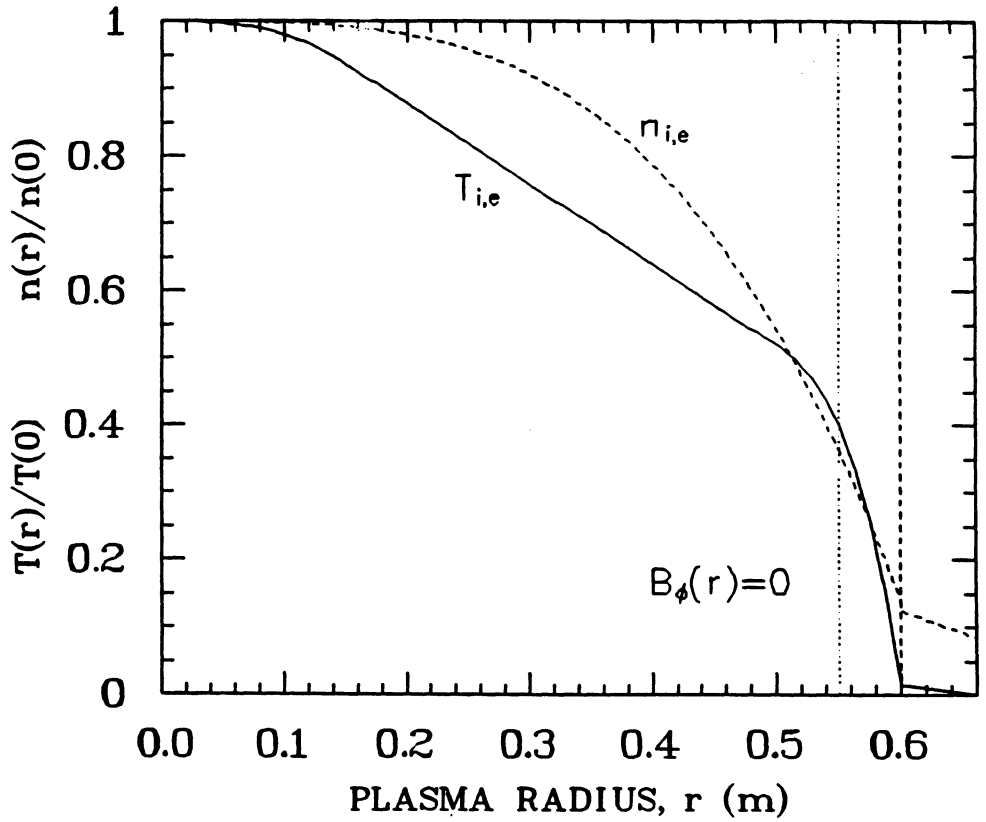

Figure 5.6-1. Radial profiles of electron temperatures, $T_e(r)$, and density, $n_e(r)$, used in the calculation of pellet injection/ablation. The reversal surface ($B_\phi = 0$ at $r_r = 0.55\,\mathrm{m}$) and plasma separatrix ($r_p = 0.60\,\mathrm{m}$) are indicated by, respectively, dotted and dashed vertical lines.

than the time for a pellet to cross the flux surface ($\tau_{pel} \simeq 5\,\mu\mathrm{s}$). The pellet, therefore, first ablates, then the particles spread out along the flux surface, and finally particles diffuse radially to readjust plasma profiles. Larger initial pellet radius or higher injection speed allows deeper penetration into the plasma. It is desirable to limit the individual-pellet particle inventory to a small fraction, g, of the nominal plasma particle inventory to reduce fluctuations in the plasma density and fusion power during refueling. Ablation caused by fusion-product alpha particles is ignorable for the shallow penetration case of interest to TITAN. If deep penetration is required, incremented injection speed must be provided to overcome the additional ablation from energetic alpha particles, although the magnitude of this effect is not well known and may, in fact, be negligible.

The time interval between pellet injections is given by

$$\tau_I \;=\; \frac{M_p}{\dot{M}_p}\,, \tag{5.6-4}$$

where $\dot{M}_p = 1.22 \times 10^{-4}\,\mathrm{kg/s}$ is the required mass flow rate and M_p is the pellet mass (with $\rho_o = 250\,\mathrm{kg/m^3}$ and $n_o = 3.18 \times 10^{28}\,\mathrm{m^{-3}}$). Pellet fueling parameters for several combinations of assumed ratios of initial pellet-to-plasma inventory, g, and normalized penetration distance, d/r_p, are summarized in Table 5.6-I. Results for the deep penetration options are included; advanced acceleration technologies would need to be developed in such cases, however. It may be desirable to synchronize the pellet injection time with the OFCD oscillation period (Section 7) to optimize profile control. As seen from the results presented in Table 5.6-I, a g-value just below 0.05 provides this benefit. An injection speed $u \simeq 2.1\,\mathrm{km/s}$ results in a penetration depth $d/r_p \simeq 0.15$, consistent with the goal of pellet deposition just inside of the reversal layer. This speed is consistent with that available from near-term acceleration technology [28].

A more advanced model [34] of pellet ablation has also been applied in the TITAN study. In this model, illustrated schematically in Figure 5.6-2, an energy balance is made at the plasma surface [34] to yield the following relationship:

$$\lambda_s^m \dot{N} \;=\; -\lambda_s^m n_s^m 4\pi a^2 \dot{a} \;=\; 4\pi a^2 Q_p\,, \tag{5.6-5}$$

where,

$$\dot{a} \;=\; -\frac{Q_p}{\lambda_s^m n_s^m}\,, \tag{5.6-6}$$

λ_s^m is the molecular heat of sublimation, $\dot{N}$ is the atomic evaporation rate at the pellet surface, n_s^m is the molecular density of the solid, a is the pellet radius, and Q_p is the effective incident energy-flux averaged over the pellet surface. All energy reaching the pellet surface is assumed to result in evaporation rather than bulk heating of the pellet (*i.e.*, energetic runaway electrons are ignored).

A detailed fit to a separate hydrodynamic solution [34,35] of the expansion of the neutral-particle ablation cloud then gives the pellet surface ablation rate,

$$\dot{a} \;=\; -\frac{1.25}{2a\,n_s^m}\int_a^{r_o} n^o\,[q^o\,a\,0.5(\gamma-1)]^{1/3}\,dl\,, \tag{5.6-7}$$

where,

$$q^o \;=\; \frac{k_B\,(Q_o - Q_p)}{2A_p\,m_p\,\int_a^{r_o} n^o\,dl}\,, \tag{5.6-8}$$

Table 5.6-I.

TITAN PELLET-FUELING PARAMETER VARIATIONS[a]

Pellet inventory/plasma inventory	0.01	0.05	0.10
Pellet radius, a (mm)	0.97	1.71	2.15
Pellet injection interval, τ_I (ms)	3.69	18.5	36.9[b]
Pellet mass, M_p (kg)	1.04×10^{-7}	5.20×10^{-6}	1.04×10^{-6}

Penetration depth, d/r_p	Pellet Speed, u (km/s)		
0.05	0.48	0.19	0.13
0.10	2.26	0.93	0.63
0.15	5.16	2.11	1.43[c]
0.20	8.80	3.59	2.45
0.25	13.1	5.34	3.63
0.50	44.1	18.0	12.3
0.75	92.6	37.9	25.8
1.00	155.2	63.5	43.2

(*a*) Fixed parameters: $n_e = 9.39 \times 10^{20}\,\mathrm{m}^{-3}$, $T_e = 9.5\,\mathrm{keV}$, $r_p = 0.60\,\mathrm{m}$, $\tau_{pi} = 3.6\,\mathrm{s}$, and DT mass injection rate, $\dot{M}_p = 2.82 \times 10^{-5}\,\mathrm{kg/s}$.

(*b*) Synchronization with the oscillations of OFCD at $f = 25\ Hz$ would imply a pellet injection interval of 40 ms at a slightly higher value of g.

(*c*) Reference case consistent with near-term acceleration technology [28].

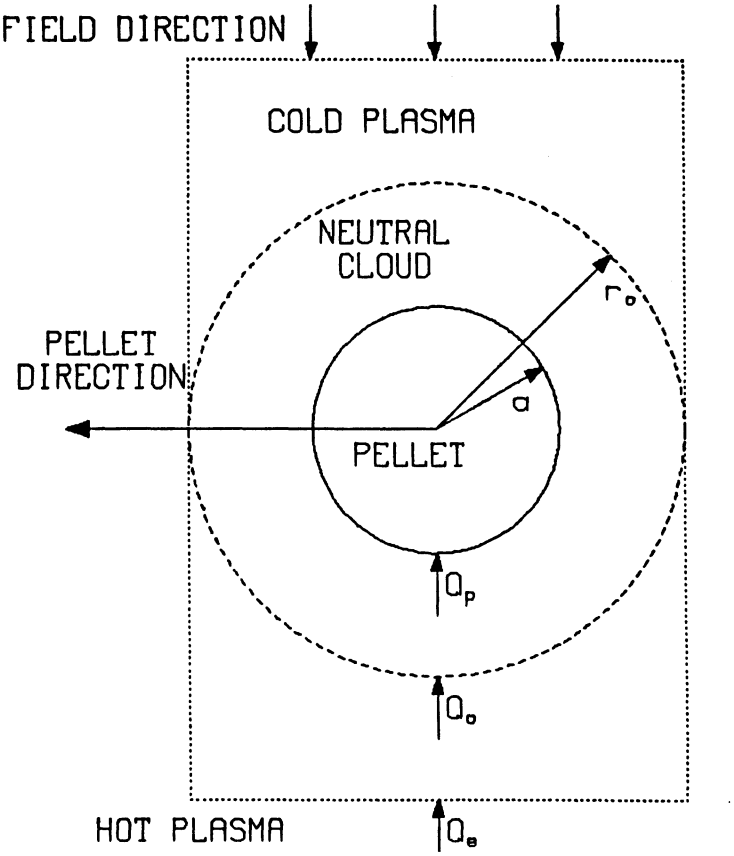

Figure 5.6-2. Schematic representation of the advanced (spherical) pellet-ablation model [34].

where q° is the net energy flux normalized to the thickness of the neutral cloud, $\gamma = 7/5$ is the ratio of specific heats for hydrogenic gas, m_p is the mass of a proton, A_p is the atomic mass number of the pellet species, Q° is the incident energy-flux averaged over the surface of the neutral cloud, n° is the atomic density in the neutral cloud, r° is the radius of the neutral cloud, and the integral represents the thickness of the neutral cloud. Additional features of the model [34] include the following:

- A multiple-energy-group (number of energy groups, NEG = 1 to 10) description of the Maxwellian electron-energy distribution at the cloud surface is used in calculating the heat flux penetrating to the pellet.
- A self-limiting-ablation model accounts for the depletion of electrons from energy groups within a flux surface.
- A cold-plasma-shielding model accounts for the cold plasma formed by ionization of the neutral particle cloud.

Results of the simple and advanced models are compared in Figure 5.6-3. Agreement is satisfactory only for the shallow penetration case of interest to applications. For deep (central) penetration, the advanced model predicts significantly higher required pellet-injection speeds and implies the required development of advanced acceleration technologies.

The local perturbations of the TITAN plasma density and temperature profiles are calculated by the advanced model and illustrated in Figure 5.6-4. As expected, density increases locally where the pellet is ablated and the edge region temperature is suppressed prior to particle diffusion and energy equilibration. Results depend upon which features of the advanced model are invoked. Best agreement between the simple and advanced model occurs (for the shallow penetration regime) when multiple-energy-group and cold-plasma-shielding effects are included; self-limiting ablation is relatively unimportant for shallow penetration.

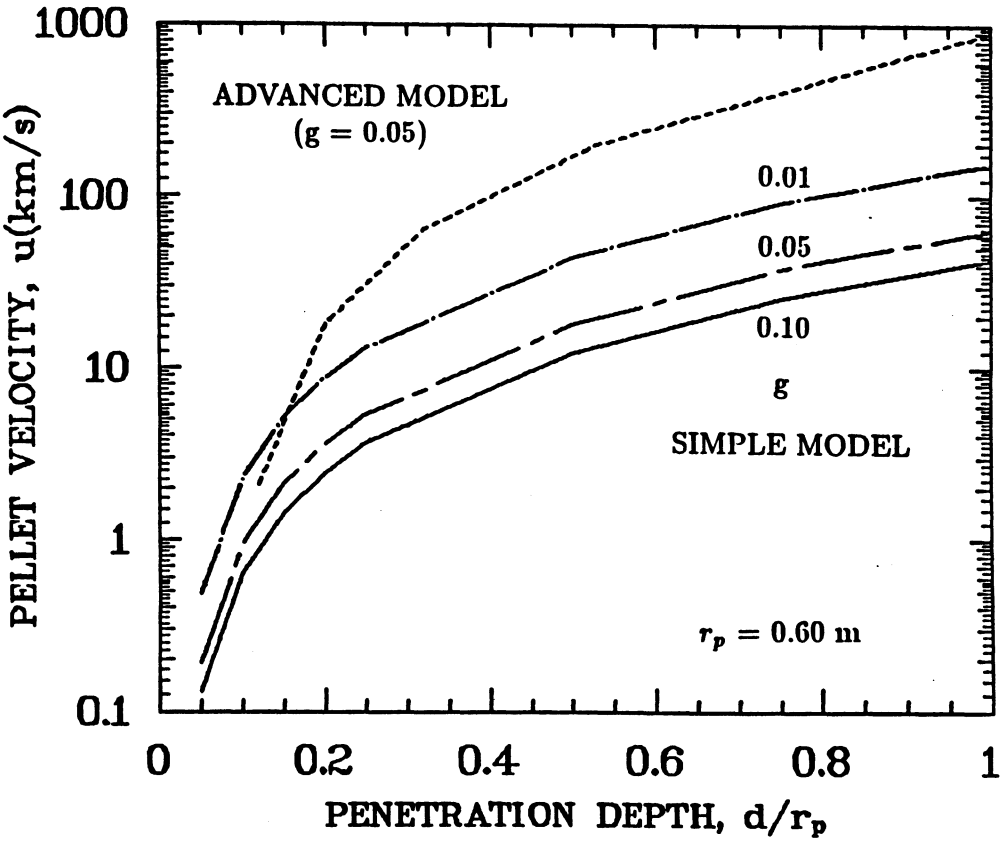

Figure 5.6-3. Comparison of pellet penetration results from the simple and advanced [34] models used in the TITAN study. Agreement is satisfactory only for the shallow penetration case of interest to TITAN.

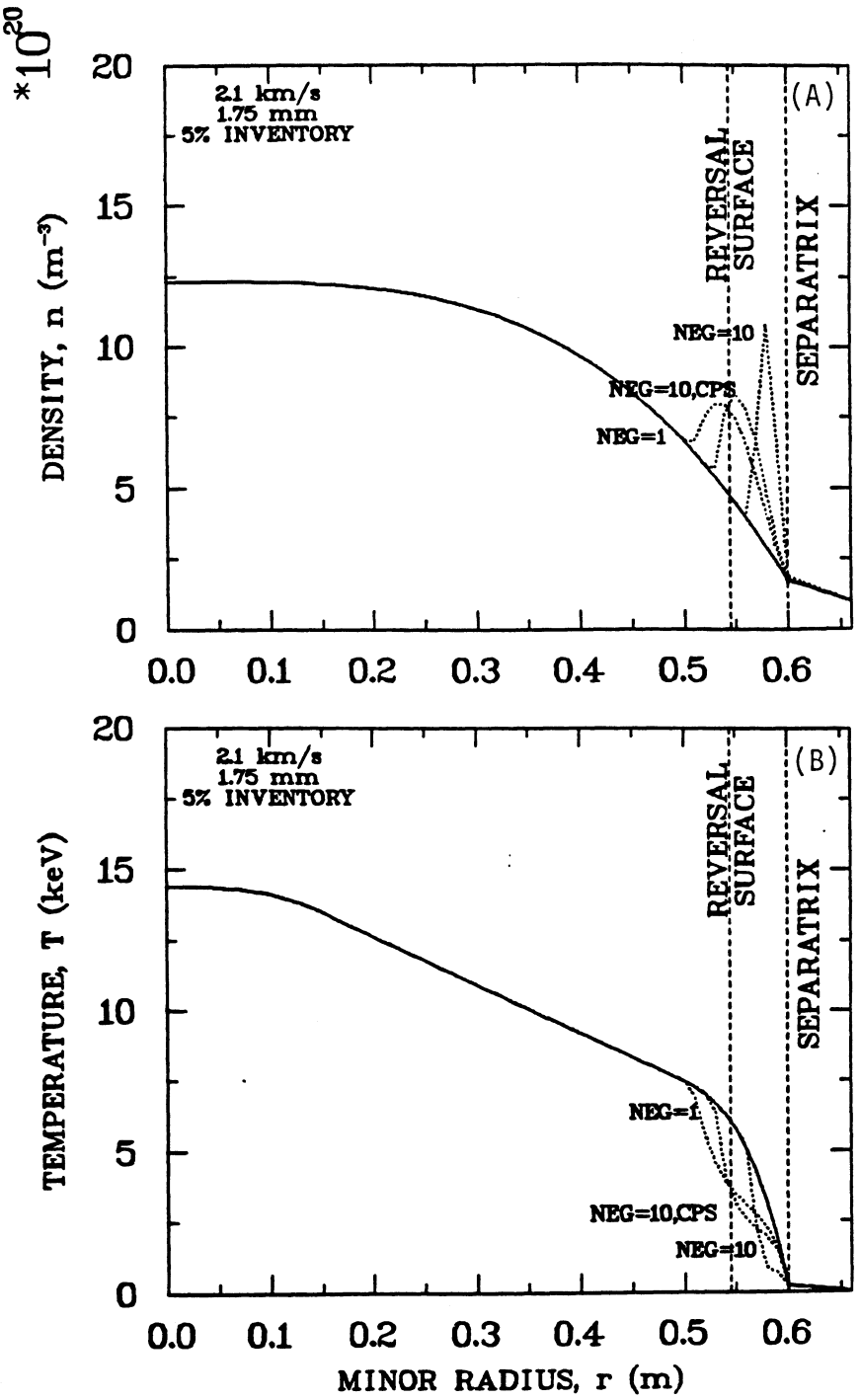

Figure 5.6-4. Local perturbation of the TITAN plasma density (A) and temperature (B) profiles caused by pellet ablation calculated by the advanced model [34]. Options invoked by the advanced model include cold plasma shielding and the number of energy groups, NEG = 1 to 10.

In summary, fueling of the TITAN RFP reactor appears to be relatively straightforward. A pellet injector based on present technology can inject 2.1-km/s pellets past the reversal radius ($r_r \simeq 0.55\,\mathrm{m}$). Presently available injector frequencies ($\sim 6\,\mathrm{Hz}$) will have to be increased to $\sim 25\,\mathrm{Hz}$ for TITAN applications. For fixed injection speed, pellets do not penetrate as far as the simple-fit model ($d = 0.07\,\mathrm{m}$ *versus* $0.09\,\mathrm{m}$ at $u = 21\,\mathrm{km/s}$), particularly for deep penetration ($d = 0.19\,\mathrm{m}$ *versus* $0.60\,\mathrm{m}$ at $u = 64\,\mathrm{km/s}$). A single large pellet penetrates as deeply as two sequential small pellets of equal total inventory. Pellets composed of TT penetrate slightly deeper than DD pellets ($d = 0.13\,\mathrm{m}$ *versus* $0.12\,\mathrm{m}$ for $u = 21\,\mathrm{km/s}$ 1.75-mm pellets), but the difference does not justify DT isotopic separation. Future work should self-consistently incorporate the pellet-refueling source profiles into the temporal 1-D, core-plasma transport description to evaluate the profile effects on global plasma characteristics. Also, a model [33] of asymmetric pellet ablation (Section 2.3.3) remains to be applied to RFP reactors.

It is assumed that TITAN will be provided with two injection systems (5 M$ each) for redundancy. The injectors themselves can be placed relatively remote from the TITAN FPC (*e.g.*, outside the vacuum task for TITAN-I or well above the TITAN-II FPC to avoid penetrations through the water pool enclosure.) Each injector would occupy an essentially cubic box with a volume of approximately one cubic meter [28]. An evacuated drift tube would connect each injector to the FPC in the vicinity of the divertors to avoid penetrations through the blanket/shield subsystems.

5.7. SUMMARY AND CONCLUSIONS

Extensive studies of the TITAN burning plasma have been performed in order to analyze the plasma behavior and performance (*e.g.*, equilibrium, stability, and transport), and to study key plasma-support systems (*e.g.*, current drive, fueling, impurity control, and particle exhaust). As a whole, these analyses provided detailed descriptions of the burning plasma for all engineering activities and design efforts. The results also provide information to the system analysis activity for improving parametric systems models that were then used to generate new cost-optimized design points for further conceptual design and analysis.

Although two separate fusion-power-core designs were studied for the TITAN reactor, lithium cooled for TITAN-I and an aqueous solution of a lithium salt as the coolant and breeder for TITAN-II, both designs had the same plasma parameters. Therefore, most of the burning-plasma simulation effort was not duplicated and, although there are certain

references specifically to the TITAN-I design, only minor modifications would be required for TITAN-II.

The TITAN burning-plasma simulations include analyses of the equilibrium and stability of the TITAN plasma (Section 5.2). These equilibrium analyses were performed using a large-aspect-ratio approximation. Two-dimensional equilibrium analysis, however, was also performed to substantiate the accuracy of such an approximation for the TITAN effort. The most important equilibrium and stability issue is the need for a conducting shell. The existence and role of a close-fitting conducting shell that surrounds the RFP strongly impacts all physics and engineering aspect of the design.

Experimental observation of the scaling of RFP plasma pressure with the toroidal current, $nT_e(0) \propto I_\phi^2$, is suggestive of operation near a β limit. Under this condition, the intrinsic transport would adjust by MHD activity, radiation, or other mechanism to lose energy at a sufficient rate to maintain β_θ constant. Taking advantage of this RFP characteristic, the TITAN plasma operates with a highly radiative core plasma, deliberately doped with Xe impurities, to reduce the heat flux on the divertor plates. One-dimensional transport simulations of the TITAN core plasma were performed to study the behavior of highly radiative core plasmas (Section 5.3). It was found that high-Z impurities are preferable since the required core-radiation fraction can be achieved with a smaller amount of impurity (and smaller Z_{eff}). Important physics issues remain that should be further explored by the RFP program. They include: (1) β-limited confinement scaling in the reactor plasma regime; (2) limit on the local beta; (3) the level and mechanism of the intrinsic transport; (4) the collapse of the temperature profile due to impurity injection; (5) the interaction of competing profile effects (*e.g.*, refueling, alpha-particle transport, $T_i : T_e : n$ split); (6) the impact of the impurities on the edge plasma and the wall (*e.g.*, sputtering, wall buildup, vacuum, and tritium systems); and (7) the effects of the impurities on the start-up transient.

The characteristics of the edge plasma have been of major importance in driving the TITAN design, and extensive simulations of the edge plasma have been undertaken during the study. To obtain a self-consistent view of the behavior of the plasma and neutral particles, this analysis has been coupled to the modeling of the core plasma (Section 5.3) and the neutral particle transport (Section 5.5). The TITAN reactors use three toroidal-field divertors with an open geometry. Edge-plasma analysis suggests that the divertor design for the TITAN high-power-density RFP reactor is feasible, provided that operation in a radiation-dominated regime is possible, with only a small fraction of the steady-state plasma heating power deposited on the divertor target. An intensely recycling ($R = 0.995$), high-density ($n_e \sim 10^{21}$ m^{-3}), low-temperature ($T_e \sim 5$ eV) stable

divertor plasma is produced, with adequate ash removal. A high-Z material is required for the divertor target in order to avoid excessive sputtering from the alpha particles even at the low plasma temperatures. This requirement has led to the inclusion of a 2-mm-thick tungsten-rhenium armour on the divertor plate. Strong radiative cooling due to the xenon impurity results in low plasma temperature at the first wall ($T_e \sim 2\,\mathrm{eV}$) so that sputtering erosion is insignificant, even accounting for a possible negative sheath at the vanadium wall. Neutral-particle transport calculations with DEGAS indicate that a negligible leakage of particles from the target to the core plasma should occur and that the neutral gas escaping to the pumps is enriched in He relative to DT by a factor ~ 3. Minimal atomic data exist for cross sections and cooling rates of high-Z elements at low plasma temperatures ($T_e \leq 100\,\mathrm{eV}$). In as much as the high radiation regime appears essential for any high-power-density reactor, an experimental program to improve this data base would be of great value.

The TITAN burning-plasma simulations incorporate the latest understanding and models developed for reversed-field pinches (RFPs), as is summarized in Section 2; in several cases, new and improved models had to be developed for the TITAN study. Because of the relative lack of theoretical and experimental data bases for RFPs, the sensitivity of the design point to various physics assumptions has also been investigated (Section 3.4.2). A detailed description of the necessary R&D areas for compact RFP reactors has also been produced and is reported in Section 8.

REFERENCES

[1] I. B. Bernstein, E. A. Frieman, M. D. Kruskal, and R. M. Kulsrud, "An Energy Principle for Hydromagnetic Stability Problems," *Proc. Royal Soc.* **244** (1958) 17.

[2] V. D. Shafranov, "Plasma Equilibrium in a Magnetic Field," *Reviews of Plasma Physics* **2**, Consultant Bureau, New York (1966) 103.

[3] D. J. Strickler, J. B. Miller, K. E. Rothe, and Y-K. M. Peng, "Equilibrium Modeling of the TFCX Poloidal Field Coil System," Oak Ridge National Laboratory report ORNL/FEDC-83-10 (1984).

[4] D. C. Robinson, "High-β Diffuse Pinch Configurations," *Plasma Phys.* **13** (1971) 439.

[5] D. C. Robinson, "Tearing-Mode-Stable Diffuse-Pinch Configurations," *Nucl. Fusion* **18** (1978) 939.

[6] J. W. Connor and J. B. Taylor, "Resistive Fluid Turbulence and Energy Confinement," *Phys. Fluids* **27** (1984) 2676.

[7] V. Antoni, D. Merlin, S. Ortolani, and R. Paccagnella, "MHD Stability Analysis of Force-Free Reversed-Field Pinch Configurations," *Nucl. Fusion* **26** (1987) 1711.

[8] A. D. Merlin, S. Ortolani, and R. Paccagnella, "Free Boundary MHD Stability Configurations," in *Proc. 14th European Conf. on Cont. Fusion and Plasma Phys.*, Madrid, Spain (June 22-26, 1987).

[9] S. Ortolani, in *Proc. Int. School of Plasma Phys. Course on Mirror-Based and Field-Reversed Approaches to Magnetic Fusion,* Varenna, Italy (1983).

[10] R. G. Watt and R. A. Nebel, "Sawteeth, Magnetic Disturbances, and Magnetic Flux Regeneration in the Reversed-Field Pinch," *Phys. Fluids* **26** (1983) 1168.

[11] R. A. Nebel, "Quasi-Steady Operation of Reversed Field Pinches," Ph. D. Thesis, University of Illinois (1980).

[12] K. A. Werley "Stable Alfvén-Wave Dynamo Action in the Reversed-Field Pinch," Ph. D. Thesis, University of Illinois (1984).

[13] M. M. Pickrell, J. A. Phillips, C. J. Buchenauer, T. Cayton, J. N. Downing, A. Haberstich, *et al.*, "Evidence for a Poloidal Beta Limit on ZT-40M," *Bull. Am. Phys. Soc.* **29** (1984) 1403.

[14] J. P. Freiberg and D. W. Hewett, "Eigenmode Analysis of Resistive MHD Stability by Matrix Shooting," *J. Plasma Phys.* **26** (1981) 177.

[15] R. S. Massey, R. G. Watt, P. G. Weber, G. A. Wurden, D. A. Baker, C. J. Buchenauer, *et al.*, "Status of the ZT-40M RFP Experimental Program," *Fusion Technol.* **8** (1) (1985) 1571.

[16] P. Thullen and K. Schoenberg (Eds.), "ZT-H Reversed Field Pinch Experiment Technical Proposal," Los Alamos National Laboratory report LA-UR-84-2602 (1984).

[17] F. Najmabadi, N. M. Ghoniem, R. W. Conn, *et al.*, "The TITAN Reversed-Field-Pinch Fusion Reactor Study: Scoping Phase Report," joint report of UCLA, General Atomics, Los Alamos National Laboratory, and Rensselaer Polytechnic Institute, UCLA-PPG-1100 (January 1987).

[18] A. K. Prinja and R. W. Conn, "An Axially-Averaged Radial Transport Model of Tokamak Edge Plasmas," *J. Nucl. Mater.* **128-129**, (1984) 135.

[19] A. K. Prinja, R. F. Schafer, R. W. Conn, and H. C. Howe, "Combined Core/Boundary Layer Transport Simulations in Tokamaks," *J. Nucl. Mater.* **145-147**, (1987) 868.

[20] A. K. Prinja, R. F. Schafer, and R. W. Conn, "Modeling of Plasma Boundary Conditions with Pump Limiters and Divertors," *Bull. Am. Phys. Soc.* **31** (1986) 1536.

[21] M. F. A. Harrison, E. S. Hotston, and A. de Matteis, "Plasma Edge Physics for NET/INTOR," NET report EUR-FU/XII-361/86/50 (1985).

[22] D. E. Post, R. V. Jensen, C. B. Tarter, W. H. Grasberger, and W. A. Lokke, "Steady-State Radiative Cooling Rates for Low-Density High-Temperature Plasmas," *Atomic and Nucl. Data Tables* **20** (1977) 397.

[23] M. Petravic, D. Heifetz, and D. E. Post, "Modelling Analyses of Tokamaks with Divertors and Pumped Limiters," *Proc. 10th Int. Conf. Plasma Phys. and Cont. Nucl. Fusion Res.*, London, U. K. (September 1984) IAEA, Vienna **2** (1985) 103.

[24] D. Heifetz, D. E. Post, M. Petravic, J. Weisheit, and G. Bateman, "A Monte-Carlo Method for Neutral-Particle Transport in Diverted Plasmas," *J. Comp. Phys.* **46** (1982) 309.

[25] P. I. H. Cooke and A. K. Prinja, "An Analytic Model for Flow Reversal in Divertor Plasmas," *Nucl. Fusion* **27** (1987) 1165.

[26] A. K. Prinja and R. W. Conn, "Theory and Modelling of Helium Enrichment in Plasma Experiments with Pump Limiters," *Nucl. Fusion* **25** (1985) 1775.

[27] S. L. Milora, "Review of Pellet Fueling," *J. Fusion Energy* **1** (1981) 15.

[28] S. L. Milora, "Plasma Fueling Program," in *Fusion Energy Division Annual Progress Report*, Oak Ridge National Laboratory report ORNL-6322 (October 1987).

[29] L. J. Perkins, S. K. Ho, and J. H. Hammer, "Deep Penetration Fueling of Reactor-Grade Plasmas with Accelerated Compact Toroids," Lawrence Livermore National Laboratory preprint UCRL-96894 (June 1987), submitted to *Nucl. Fusion.*

[30] P. B. Parks and R. J. Turnbull, "Effect of Transonic Flow in the Ablation Cloud on the Lifetime of a Solid Hydrogen Pellet in a Plasma," *Phys. Fluids* **21** (1978) 1735.

[31] R. P. Gilliard and K. Kim, "Significance of Magnetic Shielding in the Ablation of a Solid Hydrogen Pellet in a Plasma," *IEEE Trans. Plasma Sci.* **PS-8** (1980) 477.

[32] W. A. Houlberg, M. A. Iskra, H. C. Howe, and S. E. Attenberger, "Pellet-A Computer Routine for Modeling Pellet Fueling in Tokamak Plasma," Oak Ridge National Laboratory report ORNL/TM-6549 (January 1979).

[33] G. A. Wurden, P. G. Weber, R. G. Watt, C. P. Munson, J. C. Ingraham, R. B. Howell, T. E. Cayton, K. Buechl, and E. J. Nilles, "Pellet Refueling of the ZT-40M Reversed Field Pinch," *Nucl. Fusion* **27** (1987) 857.

[34] W. A. Houlberg, S. L. Milora, and S. E. Attenberger, "Neutral and Plasma Shielding Model for Pellet Ablation," Oak Ridge National Laboratory report ORNL/TM-10556 (October 1987).

[35] S. L. Milora and C. A. Foster, "A Revised Neutral Gas Shielding Model for Pellet-Plasma Interactions," *IEEE Trans. Plasma Sci.* **PS-6** (1978) 578.